Softening and Stiffening Size Effects in Free Flexural Vibration of Small-scale Cracked Beams +

Akbar Hassanpour, Hossein Darban[1]

Institute of Fundamental Technological Research, Polish Academy of Sciences, Pawińskiego 5B, 02-106 Warsaw, Poland

Abstract

Studying the dynamics of small-scale beams with cracks is crucial for damage detection and maintenance in micro- and nano-electromechanical systems. This paper studies the size-dependent free transverse vibration of miniaturized cracked beams using a local/nonlocal stress-driven gradient elasticity model. A key novelty of this model is its ability to simulate both softening and stiffening behaviors at small scales, unlike other stress-driven nonlocal models in the literature. The effect of cracks on the vibration of beams is modeled by introducing rotational and translational springs at the cracked cross-sections. The analysis considers a Timoshenko small-scale beam with an arbitrary number of cracks. To solve the problem, the beam is divided into sub-beams at the cracked cross-sections, and the higher-order equations of motion are solved for each sub-beam individually. The frequencies and associated mode shapes are derived by solving the eigenvalue problem constructed by the imposition of the standard variationally consistent and non-standard constitutive boundary and continuity conditions. The accuracy of the model is verified against experimental, molecular dynamics, and analytical results from the literature. The formulated model is further used to investigate the frequencies of intact and cracked beams with different boundary conditions. The effects of shear rigidity, boundary conditions, nonlocal parameters, crack length and location, and multiple cracks on frequencies and mode shapes are systematically analyzed.

Keywords: Frequency shift; Defect; Nonlocal gradient elasticity; size-dependence; MEMS; NEMS.

[1]**- *Corresponding author:*** *Hossein Darban*; ***E-mail addresses:*** *hdarban@ippt.pan.pl*; ***Tel.:*** *(+48) 22 826 12 81*

 Published in Journal of Sound and Vibration, available online 17 April 2025, 119135. DOI: https://doi.org/10.1016/j.jsv.2025.119135

1. Introduction

Smart devices incorporating nanostructures are characterized by exceptional mechanical performance, high precision, and low energy consumption [1]. They are being utilized across various fields of science and technology, such as bioscience, materials engineering, and mechanical engineering [2]. In some of the Micro-electromechanical systems (MEMS) and nano-electromechanical systems (NEMS), electrical elements are integrated with small-scale structures such as beams, tubes, shells, and plates to function as mass sensors, accelerometers, energy harvesters, and actuators [3–5].

The study of the mechanical responses of micro- and nanostructures is complicated by the size effect, which is not considered in the models based on classical continuum mechanics. Ignoring the size effect can lead to inaccurate modeling and design of small-scale structures. To address this shortcoming, various models based on nonclassical continuum mechanics theories have been developed to incorporate size-dependence effects in modeling miniaturized structures [6–10].

An accurate and computationally cost-effective approach for addressing size-dependence in the mechanical response of small-scale structures is based on the nonlocal theory of elasticity, originally proposed by Eringen [11]. Based on Eringen's nonlocal strain-driven model, the constitutive equation relates stress at a point to the strains at all points of the body. This theory is originally expressed in an integral form, which is challenging to solve. To address this problem, the integral formulation was transformed into a set of partial differential equations. However, a paradox has emerged between the integral and differential formulations in structural theories based on Eringen's nonlocal elasticity theory [12]. For instance, in [13], a size-independent solution was obtained for the bending behavior of Bernoulli-Euler small-scale cantilever beams.

To resolve this issue in beam formulations, the stress-driven nonlocal theory of elasticity was introduced by modifying Eringen's nonlocal constitutive equation. In this approach, the strain at each point is expressed as an integral convolution of the stresses at all points in the body, using a kernel function [14]. Although the stress-driven model is well-posed, it cannot model the softening behavior observed at micro and nanoscales, e.g., in [15]. To overcome this limitation, the model was extended to a local/nonlocal stress-driven gradient (SDGE) model [16]. By incorporating gradient length scale and mixture parameters, the SDGE model can capture both softening and stiffening behaviors in miniaturized structures. This model has gained attention and is applied to

study the mechanical responses of structures at micro and nanoscales, such as vibration [17], bending [18,19] and buckling [20,21].

Micro- and nanostructures may develop cracks due to manufacturing defects, severe loading, and environmental conditions, among other factors, which can significantly change their mechanical response. Numerous studies have explored the effects of cracks on the dynamics of micro- and nanoscale structures, such as free transverse vibrations analyses of Bernoulli-Euler [22] and functionally graded Timoshenko [23] cracked nanobeam. Furthermore, torsional vibration [24], forced vibration [25], thermal vibration [26], and wave power transmission [27] of cracked nanobeams have been also studied. It is significant to highlight that the examination of cracked micro- and nanobeams using the original version of SDGE model encountered challenges because of the absence of essential mathematical continuity conditions needed to solve the resulting boundary value problem. This obstacle was overcome when a set of kinematic continuity conditions associated with the integral form of the constitutive equation of the SDGE model was derived in [18].

To the best of the authors' knowledge, no previous study has investigated the free transverse vibrations of cracked miniaturized structures using the SDGE model. The significance of applying this model lies in its capacity to analyze both stiffening and softening behaviors exhibited by micro- and nanostructures.

In this study, the free transverse vibration of both Timoshenko and Bernoulli-Euler cracked micro- and nanobeams are investigated using the SDGE model. The structure of the present paper is as follows. Section 2 introduces the problem under consideration. In section 3, the SDGE model is developed based on Timoshenko beam theory to examine the free transverse vibrations of miniaturized beams with an arbitrary number of cracks. Section 4 details the method for solving the governing differential equations and determining the natural frequencies. The results are then presented and discussed in Section 5. This section also analyzes the effects of crack length and location on the free transverse vibrations of miniaturized beams, explores the influence of nonlocal parameters in the SDGE model on natural frequencies, and examines the impact of multiple cracks. Additionally, a brief discussion in this section addresses the observed trend of increasing natural frequencies with increasing crack length for specific values of nonlocal parameters. Finally, section 6 summarizes the key findings of the study.

2. Problem definition, assumptions

Free transverse vibration of a small-scale beam with a rectangular cross-section containing $n-1$ edge cracks is considered, as illustrated in Fig. 1. The beam has an in-plane thickness of h, out-of-plane width of b, length of L, and cross-section area of A. A Cartesian coordinate system $x-y$ is established at the mid-thickness of the beam, with the origin at the left end. A generic crack has a length a_k and is located at the position x_k $(k=1,\dots,n-1)$ along the length of the beam. The local elastic compliance of the beam is given by $C=1/EI$, where E is the Young's modulus and I is the second moment of the area. Additionally, G is shear modulus, k_τ is shear correction factor and ρ is the density of the material from which the beam is made.

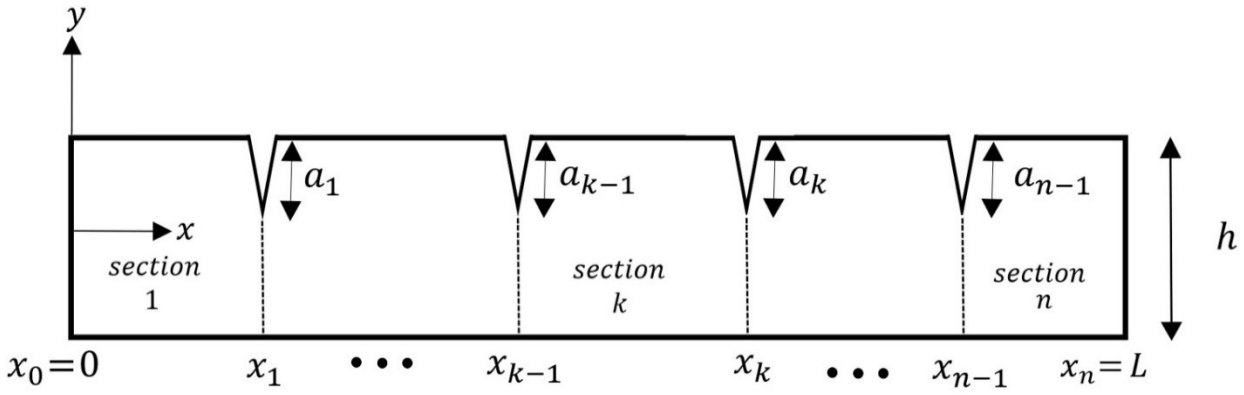

Fig. 1 Micro- or nanobeam containing multiple cracks.

In vibration studies of cracked beams, it is common to assume that cracks remain open throughout the vibration process [28–30]. This assumption simplifies the analysis by avoiding the complexities introduced by the non-linear behavior of breathing cracks [31]. In this paper, the same assumption is adopted to facilitate the calculations. Additionally, it is assumed that the cracks are sufficiently spaced apart, so their local crack tip stress fields do not interact.

The elastic spring model, depicted in Fig. 2, is frequently employed to study the impact of cracks on the mechanical behavior of structural elements such as beams and plates [32–36]. In this approach, the cracked beam is segmented into two sub-beams connected at the cracked cross-section by rotational and translational springs.

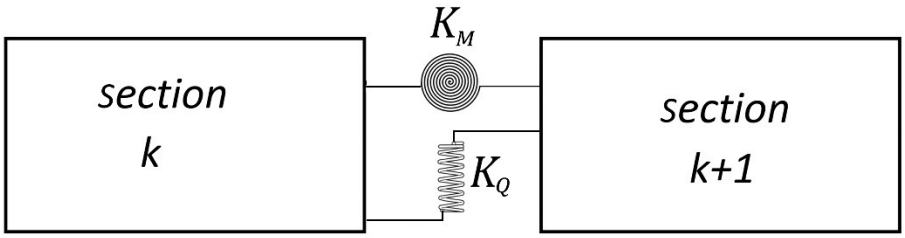

Fig. 2 Modeling crack by elastic springs.

The impact of the crack on the free transverse vibrations of cracked structures is modeled by introducing discontinuities in the cross-section rotation (θ) and transverse displacement (y) at the crack location. These discontinuities are proportional to the bending moment (M) and shear force (Q) transmitted across the crack:

$$M_{crack} = \frac{1}{C_M}(\theta_{k+1} - \theta_k) \tag{1}$$

$$Q_{crack} = \frac{1}{C_Q}(y_{k+1} - y_k) \tag{2}$$

where C_M and C_Q represent the crack compliances of the rotational and translational springs, respectively. In this paper, the closed-form solutions derived in [37] for crack compliances in a beam with a rectangular cross-section under plane stress conditions are utilized (see the Appendix).

3. Problem formulation

This section presents the SDGE model in its integral form, along with the mathematically equivalent differential equations and the required constitutive boundary and continuity conditions. Subsequently, the governing equations for free transverse vibrations of small-scale beams are derived using the equations of motions of the Timoshenko beam.

3.1. Local/nonlocal stress-driven gradient elasticity (SDGE) model

According to the local/nonlocal stress-driven gradient elasticity (SDGE) model presented in [16], the constitutive laws for a Timoshenko small-scale beam, which establishes the relationships

between the elastic curvature (χ) and the bending moment (M), as well as between the shear strain (γ) and the shear force (Q), are expressed by the following integral equations:

$$\frac{\chi(x,t)}{C} = \alpha M(x,t) + (1-\alpha)\int_0^L \phi_{L_C}(x-\zeta) M(\zeta,t)\, d\zeta - L_l^2 \frac{\partial}{\partial x}\int_0^L \phi_{L_C}(x-\zeta)\frac{\partial M(\zeta,t)}{\partial \zeta} d\zeta \tag{3}$$

$$k_\tau GA\gamma(x,t) = \alpha Q(x,t) + (1-\alpha)\int_0^L \phi_{L_C}(x-\zeta) Q(\zeta,t)\, d\zeta - L_l^2 \frac{\partial}{\partial x}\int_0^L \phi_{L_C}(x-\zeta)\frac{\partial Q(\zeta,t)}{\partial \zeta} d\zeta \tag{4}$$

where C is the local compliance, G shear modulus, k_τ shear correction factor, and A the cross-section area. The SDGE model incorporates three nonlocal parameters L_c, L_l and α. The parameter L_c represents the material length scale contributing to the stiffening behavior at micro- and nanoscales. In contrast, L_l is a gradient length scale parameter associated with the softening behavior of small-scale structures. The first two terms on the right-hand side of the integral forms of the constitutive laws, which involve the mixture parameter α, represent a combination of local and nonlocal contributions. The relative weight of these contributions is controlled by α, which ranges between 0 and 1. When $\alpha = 0$, the local contribution vanishes, resulting in a fully nonlocal response within the SDGE model. As the value of α approaches 1, the nonlocal contribution diminishes while the local contribution becomes more pronounced.

In Eq.(3) and Eq.(4), ϕ_{L_C} is a kernel function which depends on the length scale parameter L_c and often defined as:

$$\phi_{L_C}(x) = \frac{1}{2L_C} e^{\left(-\frac{|x|}{L_C}\right)} \tag{5}$$

For nanobeams with internal discontinuities, such as the one considered in this paper, the integral form of the SDGE model over the entire nanobeam length must be reformulated into a set of partial differential equations for each sub-beam, subject to mathematically consistent boundary and continuity conditions. This approach is detailed in [18], and the equations are presented below.

The integral representations of the constitutive laws in Eq.(3) and Eq.(4) are mathematically equivalent to the following differential equations for sub-beam k [18]:

$$\chi_k - L_C^2 \frac{\partial^2 \chi_k}{\partial x^2} = C M_k - C(\alpha L_C^2 + L_l^2) \frac{\partial^2 M_k}{\partial x^2} \tag{6}$$

$$\gamma_k - L_C^2 \frac{\partial^2 \gamma_k}{\partial x^2} = C_s Q_k - C_s (\alpha L_C^2 + L_l^2) \frac{\partial^2 Q_k}{\partial x^2} \tag{7}$$

for $k = 1, \ldots . n$. For simplicity, $C_s = 1/k_\tau GA$ is assumed. Here and throughout the paper, k subscript on the right side of a quantity denotes association with the section k.

This transformation of the constitutive laws leads to the following constitutive boundary conditions at both ends of small-scale beams [18]:

$$L_C^2 \frac{\partial \chi_1(0,t)}{\partial x} - L_C \chi_1(0,t) = C(\alpha L_C^2 + L_l^2) \frac{\partial M_1(0,t)}{\partial x} - C \alpha L_C M_1(0,t) \tag{8}$$

$$L_C^2 \frac{\partial \gamma_1(0,t)}{\partial x} - L_C \gamma_1(0,t) = C_s (\alpha L_C^2 + L_l^2) \frac{\partial Q_1(0,t)}{\partial x} - C_s \alpha L_C Q_1(0,t) \tag{9}$$

$$L_C^2 \frac{\partial \chi_n(L,t)}{\partial x} + L_C \chi_n(L,t) = C(\alpha L_C^2 + L_l^2) \frac{\partial M_n(L,t)}{\partial x} + C \alpha L_C M_n(L,t) \tag{10}$$

$$L_C^2 \frac{\partial \gamma_n(L,t)}{\partial x} + L_C \gamma_n(L,t) = C_s (\alpha L_C^2 + L_l^2) \frac{\partial Q_n(L,t)}{\partial x} + C_s \alpha L_C Q_n(L,t) \tag{11}$$

and constitutive continuity conditions at each cracked cross-section [18]:

$$L_C^2\frac{\partial \chi_k(x_{k-1},t)}{\partial x}-L_C\,\chi_k(x_{k-1},t)=C\,\alpha\,L_C^2\,\frac{\partial M_k(x_{k-1},t)}{\partial x}-C\,\alpha\,L_C M_k(x_{k-1},t)$$
$$-2\,C\,L_C(1-\alpha)\left[\sum_{i=1}^{k-1}\int_{x_{i-1}}^{x_i}\frac{1}{2L_C}e^{-\frac{x-\zeta}{L_C}}M_i(\zeta,t)\,d\zeta\right] \tag{12}$$
$$+2\,C\,L_C\,L_l^2\left[\frac{\partial}{\partial x}\sum_{i=1}^{k-1}\int_{x_{i-1}}^{x_i}\frac{1}{2L_C}e^{-\frac{x-\zeta}{L_C}}\frac{\partial M_i(\zeta,t)}{\partial\zeta}d\zeta+\frac{\partial}{\partial x}\int_{x_{k-1}}^{x}\frac{1}{2L_C}e^{-\frac{x-\zeta}{L_C}}\frac{\partial M_k(\zeta,t)}{\partial\zeta}d\zeta\right]$$

$$L_C^2\frac{\partial \gamma_k(x_{k-1},t)}{\partial x}-L_C\,\gamma_k(x_{k-1},t)=C_s\,\alpha\,L_C^2\,\frac{\partial Q_k(x_{k-1},t)}{\partial x}-C_s\,\alpha\,L_C Q_k(x_{k-1},t)$$
$$-2\,C_s\,L_C(1-\alpha)\left[\sum_{i=1}^{k-1}\int_{x_{i-1}}^{x_i}\frac{1}{2L_C}e^{-\frac{x-\zeta}{L_C}}Q_i(\zeta,t)\,d\zeta\right] \tag{13}$$
$$+2\,C_s\,L_C\,L_l^2\left[\frac{\partial}{\partial x}\sum_{i=1}^{k-1}\int_{x_{i-1}}^{x_i}\frac{1}{2L_C}e^{-\frac{x-\zeta}{L_C}}\frac{\partial Q_i(\zeta,t)}{\partial\zeta}d\zeta+\frac{\partial}{\partial x}\int_{x_{k-1}}^{x}\frac{1}{2L_C}e^{-\frac{x-\zeta}{L_C}}\frac{\partial Q_k(\zeta,t)}{\partial\zeta}d\zeta\right]$$

$$L_C^2\frac{\partial \chi_k(x_k,t)}{\partial x}+L_C\,\chi_k(x_k,t)=C\,\alpha\,L_C^2\,\frac{\partial M_k(x_k,t)}{\partial x}+C\,\alpha\,L_C M_k(x_k,t)$$
$$+2\,C\,L_C(1-\alpha)\left[\sum_{i=k+1}^{n}\int_{x_{i-1}}^{x_i}\frac{1}{2L_C}e^{\frac{x-\zeta}{L_C}}M_i(\zeta,t)\,d\zeta\right] \tag{14}$$
$$-2\,C\,L_C\,L_l^2\left[\frac{\partial}{\partial x}\int_{x}^{x_k}\frac{1}{2L_C}e^{\frac{x-\zeta}{L_C}}\frac{\partial M_k(\zeta,t)}{\partial\zeta}d\zeta+\frac{\partial}{\partial x}\sum_{i=k+1}^{n}\int_{x_{i-1}}^{x_i}\frac{1}{2L_C}e^{\frac{x-\zeta}{L_C}}\frac{\partial M_i(\zeta,t)}{\partial\zeta}d\zeta\right]$$

$$L_C^2\frac{\partial \gamma_k(x_k,t)}{\partial x}+L_C\,\gamma_k(x_k,t)=C_s\,\alpha\,L_C^2\,\frac{\partial Q_k(x_k,t)}{\partial x}+C_s\alpha\,L_C Q_k(x_k,t)$$
$$+2\,C_s\,L_C(1-\alpha)\left[\sum_{i=k+1}^{n}\int_{x_{i-1}}^{x_i}\frac{1}{2L_C}e^{\frac{x-\zeta}{L_C}}Q_i(\zeta,t)\,d\zeta\right] \tag{15}$$
$$-2\,C_s\,L_C\,L_l^2\left[\frac{\partial}{\partial x}\int_{x}^{x_k}\frac{1}{2L_C}e^{\frac{x-\zeta}{L_C}}\frac{\partial Q_k(\zeta,t)}{\partial\zeta}d\zeta+\frac{\partial}{\partial x}\sum_{i=k+1}^{n}\int_{x_{i-1}}^{x_i}\frac{1}{2L_C}e^{\frac{x-\zeta}{L_C}}\frac{\partial Q_i(\zeta,t)}{\partial\zeta}d\zeta\right]$$

for $k=1,\ldots.n$. For the first section ($k=1$), at its left end, the constitutive continuity conditions (12) and (13) reduce to the constitutive boundary conditions as given by Eq.(8) and Eq.(9).

Similarly, for the last section ($k = n$), at its right end, the constitutive continuity conditions (14) and (15) take the forms of the constitutive boundary conditions presented in Eq.(10) and Eq.(11). Therefore, Eqs.(12)-(15) present $4(n-1)$ non-standard constitutive continuity conditions necessary to solve the boundary value problem.

3.2. Governing differential equations for small-scale beams

According to the Timoshenko beam theory, the relationship between the shear strain $\gamma(x,t)$, transverse displacement $y(x,t)$, cross-section rotation $\theta(x,t)$ and the elastic curvature of the beam $\chi(x,t)$ are as follows:

$$\gamma_k(x,t) = \frac{\partial y_k(x,t)}{\partial x} - \theta_k(x,t) \tag{16}$$

$$\chi_k(x,t) = \frac{\partial \theta_k(x,t)}{\partial x} \tag{17}$$

The dynamic equilibrium equations for the free transverse vibration of sub-beam k based on the Timoshenko beam model are:

$$\frac{\partial Q_k(x,t)}{\partial x} = \rho A \ddot{y}_k(x,t) \tag{18}$$

$$\frac{\partial M_k(x,t)}{\partial x} + Q_k(x,t) = \rho I \ddot{\theta}_k(x,t) \tag{19}$$

where ρ is the density. Throughout this paper, the symbol $\ddot{X}$ represents the second time derivative of a given parameter X.

By taking the first derivative of Eq.(19) to define $\partial Q_k / \partial x$, and replacing the expression into Eq.(18), the following equation for the second derivative of the bending moment is obtained:

$$\frac{\partial^2 M_k(x,t)}{\partial x} = pI\frac{\partial \ddot{\theta}_k(x,t)}{\partial x} - \rho A\,\ddot{y}_k(x,t) \tag{20}$$

To obtain the equation for the bending moment, equations (17) and (20) are substituted into Eq.(6):

$$CM_k(x,t) = \frac{\partial \theta_k(x,t)}{\partial x} - L_C^2\frac{\partial^3 \theta_k(x,t)}{\partial x^3} + \rho IC(\alpha L_C^2 + L_l^2)\frac{\partial \ddot{\theta}_k(x,t)}{\partial x} - \rho AC(\alpha L_C^2 + L_l^2)\ddot{y}_k(x,t) \tag{21}$$

Additionally, taking the first derivative of Eq.(18), results in the following expression for the second derivative of the shear force:

$$\frac{\partial^2 Q_k(x,t)}{\partial x^2} = \rho A\frac{\partial \ddot{y}_k(x,t)}{\partial x} \tag{22}$$

By substituting equations (16) and (22) in Eq.(7) the equation for shear force is obtained as:

$$C_s Q_k(x,t) = \frac{\partial y_k(x,t)}{\partial x} - \theta_k(x,t) - L_C^2\left(\frac{\partial^3 y_k(x,t)}{\partial x^3} - \frac{\partial^2 \theta_k(x,t)}{\partial x^2}\right) + \rho AC_s(\alpha L_C^2 + L_l^2)\frac{\partial \ddot{y}_k(x,t)}{\partial x} \tag{23}$$

Next, taking the second derivative of Eq.(21) with respect to x and substituting it into Eq.(20) results in the first governing equation for the vibration of sub-beam k in terms of the displacement functions:

$$\begin{aligned} &L_C^2\frac{\partial^5 \theta_k(x,t)}{\partial x^5} - \frac{\partial^3 \theta_k(x,t)}{\partial x^3} - \rho IC\,(\alpha L_C^2 + L_l^2)\frac{\partial^3 \ddot{\theta}_k(x,t)}{\partial x^3} + \rho IC\frac{\partial \ddot{\theta}_k(x,t)}{\partial x} \\ &+ \rho AC\,(\alpha L_C^2 + L_l^2)\frac{\partial^2 \ddot{y}_k(x,t)}{\partial x^2} - \rho AC\,\ddot{y}_k(x,t) = 0 \end{aligned} \tag{24}$$

Using Eq.(19), the expressions for $Q_k(x,t)$ is given by:

$$Q_k(x,t) = \rho I\, \ddot{\theta}_k(x,t) - \frac{\partial M_k(x,t)}{\partial x} \tag{25}$$

Finally, by taking the first derivative of Eq.(21) to defined $\partial M_k / \partial x$, and substituting it into (25) to define Q_k and substituting it into Eq. (23), the second differential governing equation of sub-beam *k* in terms of the displacement functions is derived as:

$$\begin{aligned} &L_C^2\left(\frac{\partial^3 y_k(x,t)}{\partial x^3} - \frac{\partial^2 \theta_k(x,t)}{\partial x^2}\right) - \left(\frac{\partial y_k(x,t)}{\partial x} - \theta_k(x,t)\right) - \frac{C_s}{C}\left(\frac{\partial^2 \theta_k(x,t)}{\partial x^2} - L_C^2 \frac{\partial^4 \theta_k(x,t)}{\partial x^4}\right) \\ &-\rho I\, C_s\,(\alpha L_C^2 + L_l^2)\frac{\partial^2 \ddot{\theta}_k(x,t)}{\partial x^2} + \rho I\, C_s\, \ddot{\theta}_k(x,t) = 0 \end{aligned} \tag{26}$$

Note that the equations of motion (24) and (26) are coupled and need to be first decoupled.

4. Solution technique

The solution of the differential governing equations (24) and (26) starts by decomposing them into a harmonic time-dependent part and a spatial differential equation. Next, the equations are transformed into their dimensionless forms, and the governing equations are then decoupled. Assuming a harmonic solution, the displacement functions are:

$$\begin{aligned} y_k(x,t) &= e^{i\omega t}\, \nu_k(x) \\ \theta_k(x,t) &= e^{i\omega t}\, \varphi_k(x) \end{aligned} \tag{27}$$

where ω is the frequency.

Substituting Eq.(27) into the first and second differential governing equations, i.e. Eq.(24) and Eq.(26), results in the following spatial form of governing equations:

$$\begin{aligned} &L_C^2 \frac{d^5 \varphi_k}{dx^5} - \frac{d^3 \varphi_k}{dx^3} + \omega^2 \rho I C\,(\alpha L_C^2 + L_l^2)\frac{d^3 \varphi_k}{dx^3} - \omega^2 \rho I C \frac{d\varphi_k}{dx} - \omega^2 \rho A C\,(\alpha L_C^2 + L_l^2)\frac{d^2 \nu_k}{dx^2} \\ &+\omega^2 \rho A C \nu_k = 0 \end{aligned} \tag{28}$$

$$L_C^2\left(\frac{d^3\nu_k}{dx^3}-\frac{d^2\phi_k}{dx^2}\right)-\left(\frac{d\nu_k}{dx}-\varphi_k\right)-\frac{C_s}{C}\left(\frac{d^2\varphi_k}{dx^2}-L_C^2\frac{d^4\varphi_k}{dx^4}\right)+\omega^2\rho I\,C_s\left(\alpha L_C^2+L_l^2\right)\frac{d^2\varphi_k}{dx^2}$$
$$-\omega^2\rho I\,C_s\,\varphi_k=0 \tag{29}$$

Using the dimensionless variables given by:

$$\bar{L}=\frac{L}{L}=1;\ \bar{\nu}=\frac{\nu}{L};\ \bar{h}=\frac{h}{L};\bar{x}=\frac{x}{L};\ \bar{\zeta}=\frac{\zeta}{L};\ \bar{\varphi}=\varphi;\ \bar{\omega}=\omega L^2\sqrt{\rho AC};$$
$$\lambda_C=\frac{L_C}{L};\ \lambda_l=\frac{L_l}{L};\ \beta=\frac{CL^2}{C_s}=\frac{k_\tau GAL^2}{EI};\ \bar{C}_M=\frac{C_M}{CL};\ \bar{C}_Q=\frac{C_Q}{CL^3} \tag{30}$$

and by substituting $I=bh^3/12$ and $A=bh$, the spatial form of governing equations (28) and (29) can be expressed in dimensionless form as:

$$\lambda_C^2\frac{d^5\bar{\varphi}_k}{d\bar{x}^5}-\frac{d^3\bar{\varphi}_k}{d\bar{x}^3}+\frac{1}{12}\bar{\omega}^2\bar{h}^2\left(\alpha\lambda_C^2+\lambda_l^2\right)\frac{d^3\bar{\varphi}_k}{d\bar{x}^3}-\frac{1}{12}\bar{\omega}^2\bar{h}^2\frac{d\bar{\varphi}_k}{d\bar{x}}-\bar{\omega}^2\left(\alpha\lambda_C^2+\lambda_l^2\right)\frac{d^2\bar{\nu}_k}{d\bar{x}^2}$$
$$+\bar{\omega}^2\bar{\nu}_k=0 \tag{31}$$

$$\lambda_C^2\left(\frac{d^3\bar{\nu}_k}{d\bar{x}^3}-\frac{d^2\bar{\phi}_k}{d\bar{x}^2}\right)-\left(\frac{d\bar{\nu}_k}{d\bar{x}}-\bar{\varphi}_k\right)-\frac{1}{\beta}\left(\frac{d^2\bar{\varphi}_k}{d\bar{x}^2}-\lambda_C^2\frac{d^4\bar{\varphi}_k}{d\bar{x}^4}\right)+\frac{1}{12\beta}\bar{\omega}^2\bar{h}^2\left(\alpha\lambda_C^2+\lambda_l^2\right)\frac{d^2\bar{\varphi}_k}{d\bar{x}^2}$$
$$-\frac{1}{12\beta}\bar{\omega}^2\bar{h}^2\bar{\varphi}_k=0 \tag{32}$$

Equations (31) and (32) are coupled, as each equation includes both $\bar{\phi}_k$ and $\bar{\nu}_k$. To solve the system of differential equations and simplify the numerical solution process, the two governing differential equations are decoupled. Through a lengthy manipulation, the decoupled equations are derived as:

$$\frac{\lambda_C^2}{\kappa_5}\left[\lambda_C^2\frac{d^8\bar{\phi}_k}{d\bar{x}^8}+(\frac{\beta\kappa_3+\kappa_4}{\beta})\frac{d^6\bar{\phi}_k}{d\bar{x}^6}-(\frac{\bar{\omega}^2\,\bar{h}^2+12\kappa_1\,\kappa_4}{12})\frac{d^4\bar{\phi}_k}{d\bar{x}^4}-\kappa_2\,\kappa_4\frac{d^2\bar{\phi}_k}{d\bar{x}^2}\right]$$
$$-\frac{1}{\kappa_5}\left[\lambda_C^2\frac{d^6\bar{\phi}_k}{d\bar{x}^6}+(\frac{\beta\kappa_3+\kappa_4}{\beta})\frac{d^4\bar{\phi}_k}{d\bar{x}^4}-(\frac{\bar{\omega}^2\,\bar{h}^2+12\kappa_1\,\kappa_4}{12})\frac{d^2\bar{\phi}_k}{d\bar{x}^2}-\kappa_2\,\kappa_4\,\bar{\phi}_k\right] \tag{33}$$
$$-\lambda_C^2\frac{d^2\bar{\phi}_k}{d\bar{x}^2}+\bar{\phi}_k-\frac{1}{\beta}(\frac{d^2\bar{\phi}_k}{d\bar{x}^2}-\lambda_C^2\frac{d^4\bar{\phi}_k}{d\bar{x}^4})+\frac{\bar{h}^2\kappa_4}{12\,\beta}\frac{d^2\bar{\phi}_k}{d\bar{x}^2}-\frac{\bar{\omega}^2\,\bar{h}^2}{12\,\beta}\bar{\phi}_k=0$$

$$\bar{v}_k=\frac{\kappa_4}{\bar{\omega}^2\kappa_5}\left[\lambda_C^2\frac{d^7\bar{\phi}_k}{d\bar{x}^7}+(\frac{\beta\kappa_3+\kappa_4}{\beta})\frac{d^5\bar{\phi}_k}{d\bar{x}^5}-(\frac{\bar{\omega}^2\,\bar{h}^2+12\kappa_1\,\kappa_4}{12})\frac{d^3\bar{\phi}_k}{d\bar{x}^3}-\kappa_2\,\kappa_4\frac{d\bar{\phi}_k}{d\bar{x}}\right]$$
$$-\frac{\lambda_C^2}{\bar{\omega}^2}\frac{d^5\bar{\phi}_k}{d\bar{x}^5}+\frac{1}{\bar{\omega}^2}\frac{d^3\bar{\phi}_k}{d\bar{x}^3}-\frac{\bar{h}^2\kappa_4}{12\bar{\omega}^2}\frac{d^3\bar{\phi}_k}{d\bar{x}^3}+\frac{\bar{h}^2}{12}\frac{d\bar{\phi}_k}{d\bar{x}} \tag{34}$$

where:

$$\kappa_1=\frac{12\lambda_C^2\,\beta+12-\bar{\omega}^2\,\bar{h}^2\,(\alpha\,\lambda_C^2+\lambda_l^2)}{12\,\lambda_C^2\,\beta}$$
$$\kappa_2=\frac{\bar{\omega}^2\,\bar{h}^2-12\beta}{12\,\lambda_C^2\,\beta}$$
$$\kappa_3=\frac{\bar{\omega}^2\,\bar{h}^2(\alpha\,\lambda_C^2+\lambda_l^2)-12}{12} \tag{35}$$
$$\kappa_4=\bar{\omega}^2\,(\alpha\,\lambda_C^2+\lambda_l^2)$$
$$\kappa_5=\frac{\bar{\omega}^2(\alpha\,\lambda_C^2+\lambda_l^2)-\bar{\omega}^2\lambda_C^2}{\lambda_C^2}$$

Equation (33) is a differential equation of order eight. Therefore, the solution of the cross-section rotation of sub-beam *k*, $\bar{\phi}_k$, depends on eight unknown constants. Once defined, $\bar{\phi}_k$ will be substituted in the algebraic equation (34) to determine the transverse displacement of the sub-beam *k*. Therefore, for a small-scale beam with $n-1$ cracks, the solution of the equations of motion depends on $8n$ unknown constants.

Additionally, applying the dimensionless variables to Eq.(21) and Eq.(23) yields the dimensionless form of the bending moment and shear force as follows:

$$\bar{M}_k = \frac{CL\,M_k}{e^{i\omega t}} = \frac{d\bar{\phi}_k}{d\bar{x}} - \lambda_C^2 \frac{d^3\bar{\phi}_k}{d\bar{x}^3} - \frac{1}{12}\bar{\omega}^2\,\bar{h}^2(\alpha\,\lambda_C^2 + \lambda_l^2)\frac{d\bar{\phi}_k}{d\bar{x}} + \bar{\omega}^2(\alpha\,\lambda_C^2 + \lambda_l^2)\bar{v}_k \tag{36}$$

$$\bar{Q}_k = \frac{CL^2 Q_k}{e^{i\omega t}} = \beta\left(\frac{d\bar{v}_k}{d\bar{x}} - \bar{\varphi}_k\right) - \beta\,\lambda_C^2\left(\frac{d^3\bar{v}_k}{d\bar{x}^3} - \frac{d^2\bar{\varphi}_k}{d\bar{x}^2}\right) - \bar{\omega}^2(\alpha\,\lambda_C^2 + \lambda_l^2)\bar{v}_k \tag{37}$$

Furthermore, the dimensionless forms of the constitutive boundary and continuity conditions, as given in Eqs.(8)-(15), are:

$$\lambda_C^2\frac{d^2\bar{\varphi}_1}{d\bar{x}^2} - \lambda_C\frac{d\bar{\varphi}_1}{d\bar{x}} - (\alpha\,\lambda_C^2 + \lambda_l^2)\frac{d\bar{M}_1}{d\bar{x}} + \alpha\,\lambda_C\bar{M}_1 = 0 \qquad at \quad \bar{x} = 0 \tag{38}$$

$$\lambda_C^2\left(\frac{d^2\bar{v}_1}{d\bar{x}^2} - \frac{d\bar{\varphi}_1}{d\bar{x}}\right) - \lambda_C\left(\frac{d\bar{v}_1}{d\bar{x}} - \bar{\varphi}_1\right) - \frac{1}{\beta}(\alpha\,\lambda_C^2 + \lambda_l^2)\frac{d\bar{Q}_1}{d\bar{x}} + \frac{1}{\beta}\alpha\,\lambda_C\bar{Q}_1 = 0 \qquad at \quad \bar{x} = 0 \tag{39}$$

$$\lambda_C^2\frac{d^2\bar{\varphi}_n}{d\bar{x}^2} + \lambda_C\frac{d\bar{\varphi}_n}{d\bar{x}} - (\alpha\,\lambda_C^2 + \lambda_l^2)\frac{d\bar{M}_n}{d\bar{x}} - \alpha\,\lambda_C\bar{M}_n = 0 \qquad at \quad \bar{x} = 1 \tag{40}$$

$$\lambda_C^2\left(\frac{d^2\bar{v}_n}{d\bar{x}^2} - \frac{d\bar{\varphi}_n}{d\bar{x}}\right) + \lambda_C\left(\frac{d\bar{v}_n}{d\bar{x}} - \bar{\varphi}_n\right) - \frac{1}{\beta}(\alpha\,\lambda_C^2 + \lambda_l^2)\frac{d\bar{Q}_n}{d\bar{x}} - \frac{1}{\beta}\alpha\,\lambda_C\bar{Q}_n = 0 \qquad at \quad \bar{x} = 1 \tag{41}$$

and

$$\begin{aligned}
&\lambda_C^2\frac{d^2\bar{\varphi}_k}{d\bar{x}^2} - \lambda_C\frac{d\bar{\varphi}_k}{d\bar{x}} - \alpha\,\lambda_C^2\frac{d\bar{M}_k}{d\bar{x}} + \alpha\,\lambda_C\bar{M}_k + (1-\alpha)\left[\sum_{i=1}^{k-1}\int_{\bar{x}_{i-1}}^{\bar{x}_i} e^{-\frac{\bar{x}-\bar{\zeta}}{\lambda_C}}\bar{M}_i(\bar{\zeta})\,d\bar{\zeta}\right] \qquad at \quad \bar{x} = \bar{x}_{k-1} \\
&-\lambda_l^2\left[\frac{d}{d\bar{x}}\sum_{i=1}^{k-1}\int_{\bar{x}_{i-1}}^{\bar{x}_i} e^{-\frac{\bar{x}-\bar{\zeta}}{\lambda_C}}\frac{d\bar{M}_i(\bar{\zeta})}{d\bar{\zeta}}\,d\bar{\zeta} + \frac{d}{d\bar{x}}\int_{\bar{x}_{k-1}}^{\bar{x}} e^{-\frac{\bar{x}-\bar{\zeta}}{\lambda_C}}\frac{d\bar{M}_k(\bar{\zeta})}{d\bar{\zeta}}\,d\bar{\zeta}\right] = 0
\end{aligned} \tag{42}$$

$$\lambda_C^2\left(\frac{d^2\bar{v}_k}{d\bar{x}^2}-\frac{d\bar{\varphi}_k}{d\bar{x}}\right)-\lambda_C\left(\frac{d\bar{v}_k}{d\bar{x}}-\bar{\varphi}_k\right)-\frac{1}{\beta}\alpha\lambda_C^2\frac{d\bar{Q}_k}{d\bar{x}}+\frac{1}{\beta}\alpha\lambda_C\bar{Q}_k$$
$$+\frac{1}{\beta}(1-\alpha)\left[\sum_{i=1}^{k-1}\int_{\bar{x}_{i-1}}^{\bar{x}_i}e^{-\frac{\bar{x}-\bar{\zeta}}{\lambda_C}}\bar{Q}_i(\bar{\zeta})\,d\bar{\zeta}\right] \qquad at\quad \bar{x}=\bar{x}_{k-1} \tag{43}$$
$$-\frac{1}{\beta}\lambda_l^2\left[\frac{d}{d\bar{x}}\sum_{i=1}^{k-1}\int_{\bar{x}_{i-1}}^{\bar{x}_i}e^{-\frac{\bar{x}-\bar{\zeta}}{\lambda_C}}\frac{d\bar{Q}_i(\bar{\zeta})}{d\bar{\zeta}}d\bar{\zeta}+\frac{d}{d\bar{x}}\int_{\bar{x}_{k-1}}^{\bar{x}}e^{-\frac{\bar{x}-\bar{\zeta}}{\lambda_C}}\frac{d\bar{Q}_k(\bar{\zeta})}{d\bar{\zeta}}d\bar{\zeta}\right]=0$$

$$\lambda_C^2\frac{d^2\bar{\varphi}_k}{d\bar{x}^2}+\lambda_C\frac{d\bar{\varphi}_k}{d\bar{x}}-\alpha\lambda_C^2\frac{d\bar{M}_k}{d\bar{x}}-\alpha\lambda_C\bar{M}_k-(1-\alpha)\left[\sum_{i=k+1}^{n}\int_{\bar{x}_{i-1}}^{\bar{x}_i}e^{\frac{\bar{x}-\bar{\zeta}}{\lambda_C}}\bar{M}_i(\bar{\zeta})\,d\bar{\zeta}\right] \qquad at\quad \bar{x}=\bar{x}_k$$
$$+\lambda_l^2\left[\frac{d}{d\bar{x}}\int_{\bar{x}}^{\bar{x}_k}e^{\frac{\bar{x}-\bar{\zeta}}{\lambda_C}}\frac{d\bar{M}_k(\bar{\zeta})}{d\bar{\zeta}}d\bar{\zeta}+\frac{d}{d\bar{x}}\sum_{i=k+1}^{n}\int_{\bar{x}_{i-1}}^{\bar{x}_i}e^{\frac{\bar{x}-\bar{\zeta}}{\lambda_C}}\frac{d\bar{M}_i(\bar{\zeta})}{d\bar{\zeta}}d\bar{\zeta}\right]=0 \tag{44}$$

$$\lambda_C^2\left(\frac{d^2\bar{v}_k}{d\bar{x}^2}-\frac{d\bar{\varphi}_k}{d\bar{x}}\right)+\lambda_C\left(\frac{d\bar{v}_k}{d\bar{x}}-\bar{\varphi}_k\right)-\frac{1}{\beta}\alpha\lambda_C^2\frac{d\bar{Q}_k}{d\bar{x}}-\frac{1}{\beta}\alpha\lambda_C\bar{Q}_k$$
$$-\frac{1}{\beta}(1-\alpha)\left[\sum_{i=k+1}^{n}\int_{\bar{x}_{i-1}}^{\bar{x}_i}e^{\frac{\bar{x}-\bar{\zeta}}{\lambda_C}}\bar{Q}_i(\bar{\zeta})\,d\bar{\zeta}\right] \qquad at\quad \bar{x}=\bar{x}_k \tag{45}$$
$$+\frac{1}{\beta}\lambda_l^2\left[\frac{d}{d\bar{x}}\int_{\bar{x}}^{\bar{x}_k}e^{\frac{\bar{x}-\bar{\zeta}}{\lambda_C}}\frac{d\bar{Q}_k(\bar{\zeta})}{d\bar{\zeta}}d\bar{\zeta}+\frac{d}{d\bar{x}}\sum_{i=k+1}^{n}\int_{\bar{x}_{i-1}}^{\bar{x}_i}e^{\frac{\bar{x}-\bar{\zeta}}{\lambda_C}}\frac{d\bar{Q}_i(\bar{\zeta})}{d\bar{\zeta}}d\bar{\zeta}\right]=0$$

for $k = 1, \ldots . n$.

For the first section ($k = 1$), the constitutive continuity conditions (42) and (43) at its left end simplify to the constitutive boundary conditions given by Eq.(38) and Eq.(39). Likewise, for the last section ($k = n$), the constitutive continuity conditions (44) and (45) at its right end reduce to the constitutive boundary conditions shown in Eq.(40) and Eq.(41).

Moreover, the variationally consistent continuity conditions at each cracked cross-section, expressed in terms of the dimensionless parameters, are:

$$
\begin{aligned}
&\bar{v}_{k+1} - \bar{v}_k = (\bar{C}_Q)_k\,(\bar{Q}_{crack})_k \\
&\bar{\varphi}_{k+1} - \bar{\varphi}_k = (\bar{C}_M)_k\,(\bar{M}_{crack})_k \qquad\qquad at \quad \bar{x} = \bar{x}_k \\
&\bar{M}_k = \bar{M}_{k+1} \\
&\bar{Q}_k = \bar{Q}_{k+1}
\end{aligned}
\tag{46}
$$

for $k = 1, \ldots . n-1$.

Finally, the dimensionless boundary conditions at both ends of the beam, determined by the type of supports, are as follows:

Table 1

The variationally consistent boundary conditions in dimensionless form.

Type of boundary	Boundary conditions	
	at $\bar{x} = 0$	at $\bar{x} = 1$
simply-supported	$\bar{v}_1 = 0$ $\bar{M}_1 = 0$	$\bar{v}_n = 0$ $\bar{M}_n = 0$
fully-clamped	$\bar{v}_1 = 0$ $\bar{\varphi}_1 = 0$	$\bar{v}_n = 0$ $\bar{\varphi}_n = 0$
cantilever	$\bar{v}_1 = 0$ $\bar{\varphi}_1 = 0$	$\bar{Q}_n = 0$ $\bar{M}_n = 0$
clamped-pinned	$\bar{v}_1 = 0$ $\bar{\varphi}_1 = 0$	$\bar{v}_n = 0$ $\bar{M}_n = 0$

As mentioned above, the solution of the equations of motion depends on $8n$ unknown constants. Solving these equations requires $8n$ boundary and continuity conditions, which consist of:

- $4(n-1)$ constitutive continuity conditions at $n-1$ cracked cross-sections, given in Eqs.(42)-(45),

- $4(n-1)$ variationally consistent continuity conditions at $n-1$ cracked cross-sections, given in Eq.(46),
- 4 constitutive boundary conditions at both ends of the beam, given in Eqs.(38)-(41),
- 4 variationally consistent boundary conditions at both ends of the beam, given in table 1.

This results in a homogeneous system of $8n$ algebraic equations for $8n$ unknown constants. The non-trivial solution exists only if the determinant of the coefficient matrix vanishes, which leads to the determination of the natural frequencies of the cracked Timoshenko micro- or nanobeam. Note that the formulated model reduces to a Bernoulli-Euler beam formulation for very large values of shear rigidity, $\beta \to \infty$.

5. Results and discussion

The developed SDGE model is employed to investigate free transverse vibrations of both Timoshenko and Bernoulli-Euler cracked small-scale beams under various boundary conditions, including simply-supported, fully-clamped, cantilever, and clamped-pinned. Natural frequencies are numerically calculated using the method described in Section 4 considering the presence of single and multiple cracks.

The model is first verified by comparing its results with experimental, theoretical, and molecular dynamics (MD) data available in the literature for both intact and cracked small-scale beams. Next, the impact of shear rigidity on the natural frequencies is explored. Following this, the effects of crack length and location are investigated. The influence of nonlocal parameters is then examined, along with the effect of multiple cracks on the natural frequencies. Finally, a discussion on the distinct trend of increasing natural frequencies with increasing crack length within the SDGE model is presented. In this section, ω_i represents the *i*-th natural frequency.

5.1. Verification

In Fig. 3, the results of the present model for Bernoulli-Euler beam formulation ($\beta \to \infty$) are compared with the experimental data from [38] for a large-scale cantilever beam with a thickness-to-length ratio of $\bar{h} = 0.039$ and containing a single crack. The ratios between the first three natural frequencies of the cracked large-scale beam and the corresponding frequencies of the intact beam (ω_{intact}) with varying dimensionless crack length ($\xi_1 = a_1/h$) are presented for different

dimensionless crack locations ($\bar{x}_1$). For the first mode, the crack is located at $\bar{x}_1 = 0.2$, while for the second and third mode, it is positioned at $\bar{x}_1 = 0.025$.

By setting the dimensionless nonlocal parameters to $\lambda_l = 0$ and $\alpha = 1$, the SDGE model can also be applied to study the free transverse vibrations of large-scale (local) beams. As the diagrams indicate, the results of the SDGE model are in good agreement with the experimental data for the first three modes of free transverse vibrations. In line with the experimental observations at the macroscale, the SDGE model accurately captures the trend of decreasing natural frequencies with increasing crack length for all vibration modes.

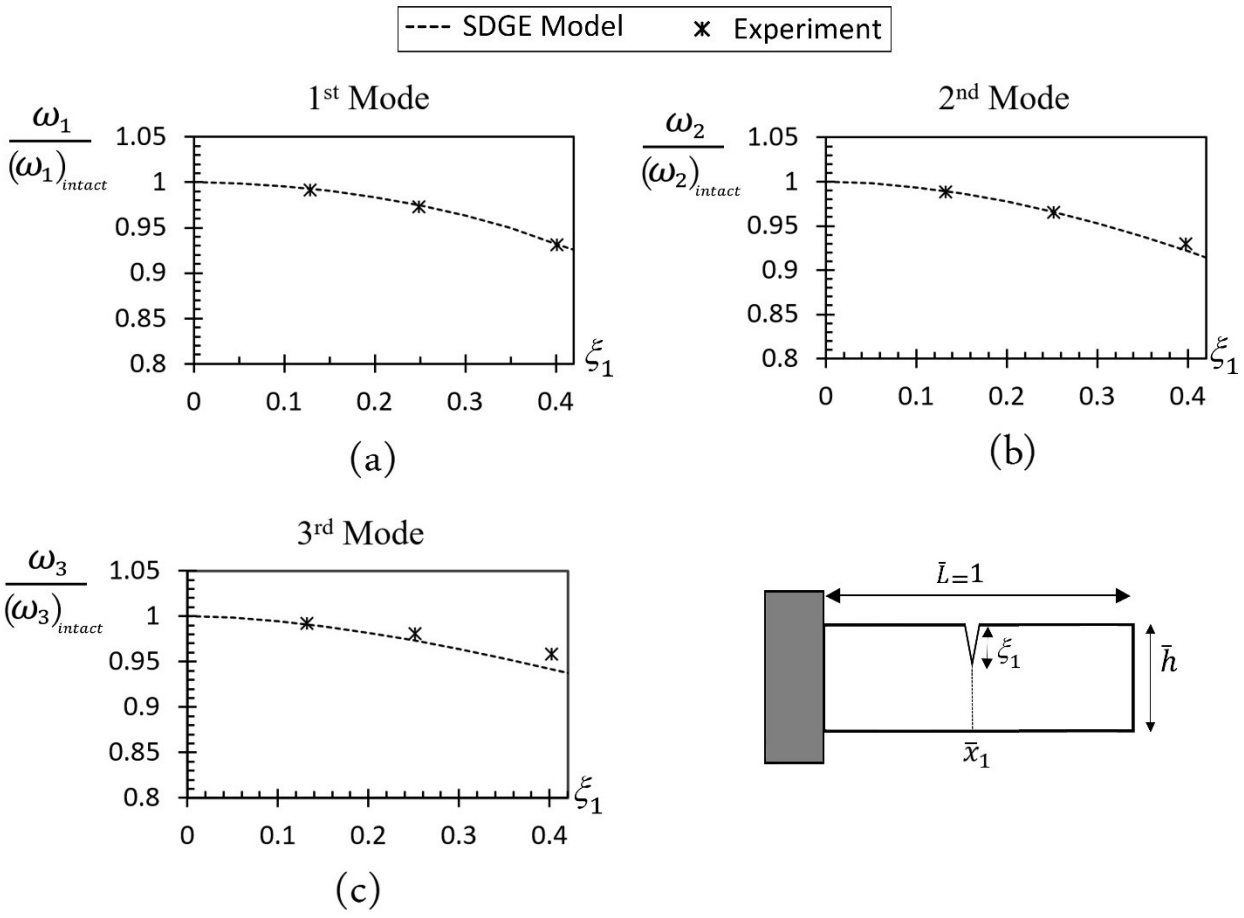

Fig. 3 The ratios between the first three natural frequencies of cracked and intact Bernoulli-Euler beam with varying crack length ξ_1. The results of the SDGE model with $\lambda_l = 0$, $\alpha = 1$ and $\beta \to \infty$ are compared with the experimental data reported by [38] for a large-scale cantilever beam with $\bar{h} = 0.039$. (a) first natural frequencies for a crack located at $\bar{x}_1 = 0.2$, (b) second natural frequencies for a crack located at $\bar{x}_1 = 0.025$, (c) third natural frequencies for a crack located at $\bar{x}_1 = 0.025$.

In Fig. 4, the MD results reported in [39] for the free transverse vibrations of an intact small-scale cantilever beam with varying lengths are used to verify the formulated SDGE model. The nanobeam in the MD simulations has a square cross-section with $\bar{h} = 1/6$, and is composed of a single-crystal silicon, oriented along the [100] lattice direction, with Young's modulus of $E =$ 99.16 GPa, density of $\rho = 2330\,{}^{\mathrm{kg}}/_{\mathrm{m}^3}$ and Poisson's ratio of $\nu = 0.28$. Using these dimensions and material properties, the dimensionless shear rigidity is calculated as $\beta = 140$.

To perform this comparison, the first natural frequencies obtained from MD simulations were used to calibrate the current SDGE model, as shown in Fig. 4. This calibration involved testing various values for the nonlocal parameters L_C, L_l, and α and comparing the obtained results with those from the MD simulations.

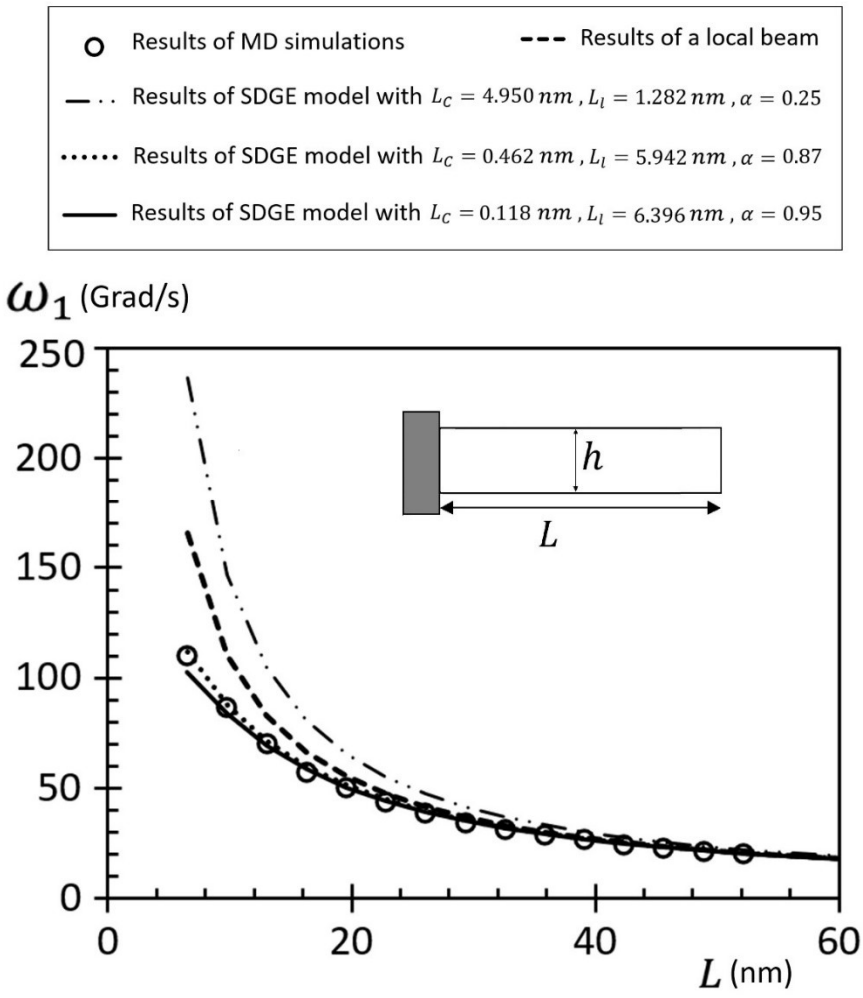

Fig. 4 First natural frequencies of an intact small-scale cantilever beam with varying beam length L. The results of SDGE model with $\beta = 140$ and various nonlocal parameters (L_C, L_l and α) are compared against those of the local beam and MD simulations reported in [39]. The MD results refer to a single-crystal silicon beam with a square cross-section and $\bar{h} = 1/6$, oriented along the [100] lattice direction, with Young's modulus of $E = 99.16$ GPa, density of $\rho = 2330\ {}^{\mathrm{kg}}/_{\mathrm{m}^3}$ and Poisson's ratio of $\nu = 0.28$.

As shown in the diagram, different values of the nonlocal parameters lead to predictions of different behaviors at the nanoscale. For instance, with $L_C = 4.950$ nm, $L_l = 1.282$ nm, and $\alpha = 0.25$, a stiffening behavior is observed, as the natural frequencies in this case are higher than those of the local beam. For example, for a nanobeam with a length of 6.52 nm, the first natural frequency obtained by the SDGE model is $\omega_1 = 236.28$ Grad/s, which is 42.5% greater than that of the local beam, $\omega_1 = 165.80$ Grad/s.

Conversely, a softening behavior is evident for the cases with $L_C = 0.462$ nm, $L_l = 5.942$ nm, $\alpha = 0.87$ and $L_C = 0.118$ nm, $L_l = 6.396$ nm, $\alpha = 0.95$, where the natural frequencies in these cases are lower than those of the local beam. Notably, the SDGE model with $L_C = 0.462$ nm, $L_l = 5.942$ nm, $\alpha = 0.87$ more accurately captures the MD results, as demonstrated in the diagram. The results in Fig. 4 demonstrate the capabilities of the SDGE model to accurately predict the natural frequencies of intact nanobeams predicted by the MD simulations.

As shown in Fig. 4, the size effect is more pronounced in shorter nanobeams. For instance, for a nanobeam with a length of 6.52 nm, the first natural frequency obtained from the calibrated SDGE model is $\omega_1 = 111.75$ Grad/s, which is 32.6% lower than that of a local beam. Additionally, as the length of the nanobeam increases, the natural frequencies gradually converge to the first natural frequencies of an intact local cantilever beam. This suggests that the size effect diminishes with increasing nanobeam length.

The accuracy of the current model is evaluated by comparing its results with those reported in [40], which employed the SDGE model to study the free transverse vibrations of Bernoulli-Euler small-scale beams without cracks. By setting the dimensionless shear rigidity parameter to infinity ($\beta \to \infty$), the present model can be applied to the Bernoulli-Euler beams at the micro- and nanoscale.

Fig. 5 presents the normalized natural frequencies of a fully-clamped Bernoulli-Euler small-scale intact beam with $\bar{h} = 0.1$, for $\lambda_l = 0.1$ and $\alpha = 0$, as well as for $\lambda_l = 0.5$ and $\alpha = 0$, with varying dimensionless length scale parameter λ_C. The natural frequencies are normalized by computing

the ratio of the first natural frequency of the small-scale beam to the corresponding frequency of the local beam, denoted as $(\omega_1)_{Loc}$. The diagrams clearly show that the normalized natural frequencies calculated using the presented SDGE model for Timoshenko beams with $\beta \to \infty$ align very well with those obtained using the SDGE model for Bernoulli-Euler intact beams in [40].

As observed, increasing the dimensionless length scale parameter λ_C leads to an increase in the normalized natural frequencies. This is attributed to the stiffening behavior exhibited by micro- and nanostructures as λ_C increase. For instance, with $\lambda_l = 0.1$ and $\alpha = 0$, when λ_c increases from 0.2 to 0.6, the frequency ratio in Fig. 5 increases from 1.5956 to 3.650, indicating a significant increase of 128.75 %.

Conversely, the dimensionless gradient length parameter λ_l has the opposite effect. As λ_l increases, it causes a softening behavior in small-scale structures, resulting in a decrease in the normalized natural frequencies. For example, with $\lambda_c = 0.6$ and $\alpha = 0$, increasing λ_l from 0.1 to 0.5 results in a reduction of the frequency ratio in Fig. 5 from 3.650 to 1.3118, representing a decrease of 64 %.

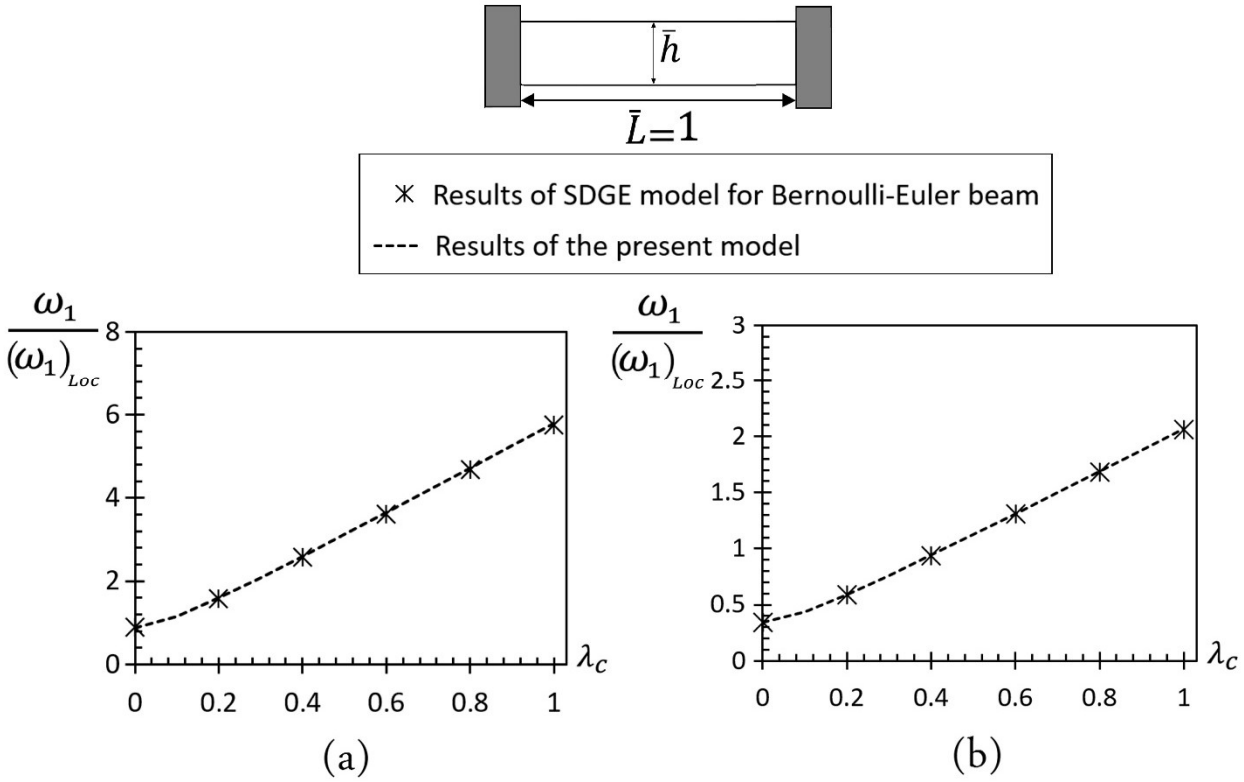

Fig. 5 The ratios between the first natural frequencies of an intact small-scale beam and intact local beam with varying dimensionless length scale parameter λ_C. The results of SDGE model with $\beta \to \infty$ are compared with the results reported in [40] for a fully-clamped Bernoulli-Euler beam with $\bar{h} = 0.1$, and dimensionless nonlocal parameters (a) $\lambda_l = 0.1$ and $\alpha = 0$ and (b) $\lambda_l = 0.5$ and $\alpha = 0$.

By setting the dimensionless gradient length parameter and the mixture parameter to zero ($\lambda_l = 0$ and $\alpha = 0$) and $\beta \to \infty$, the formulated SDGE model simplifies to a Bernoulli-Euler stress-driven model. The results of the SDGE model for the first three modes of free transverse vibration of a Bernoulli-Euler miniaturized beam with $\bar{h} = 0.1$ and clamped-pinned boundary conditions, including a crack of varying length located at $\bar{x}_1 = 0.3$, are compared, as shown in Fig. 6 , with those of the stress-driven model reported in [41]. The results are presented for the dimensionless nonlocal parameters $\lambda_C = 0.5$, $\lambda_l = 0$ and $\alpha = 0$, and $\beta \to \infty$.

The SDGE model then depends solely on the dimensionless length scale parameter λ_C, which only captures the stiffening behavior in small-scale structures. As can be seen, the results of both models are in good agreement. The minor differences, particularly for the third mode, are attributed to the inclusion of the rotary inertia term in the derivation of the SDGE model in this paper, a term that was not considered in [41]. The results show that increasing the crack length reduces all the natural frequencies, with a more significant decrease observed in the second and third dimensionless natural frequencies.

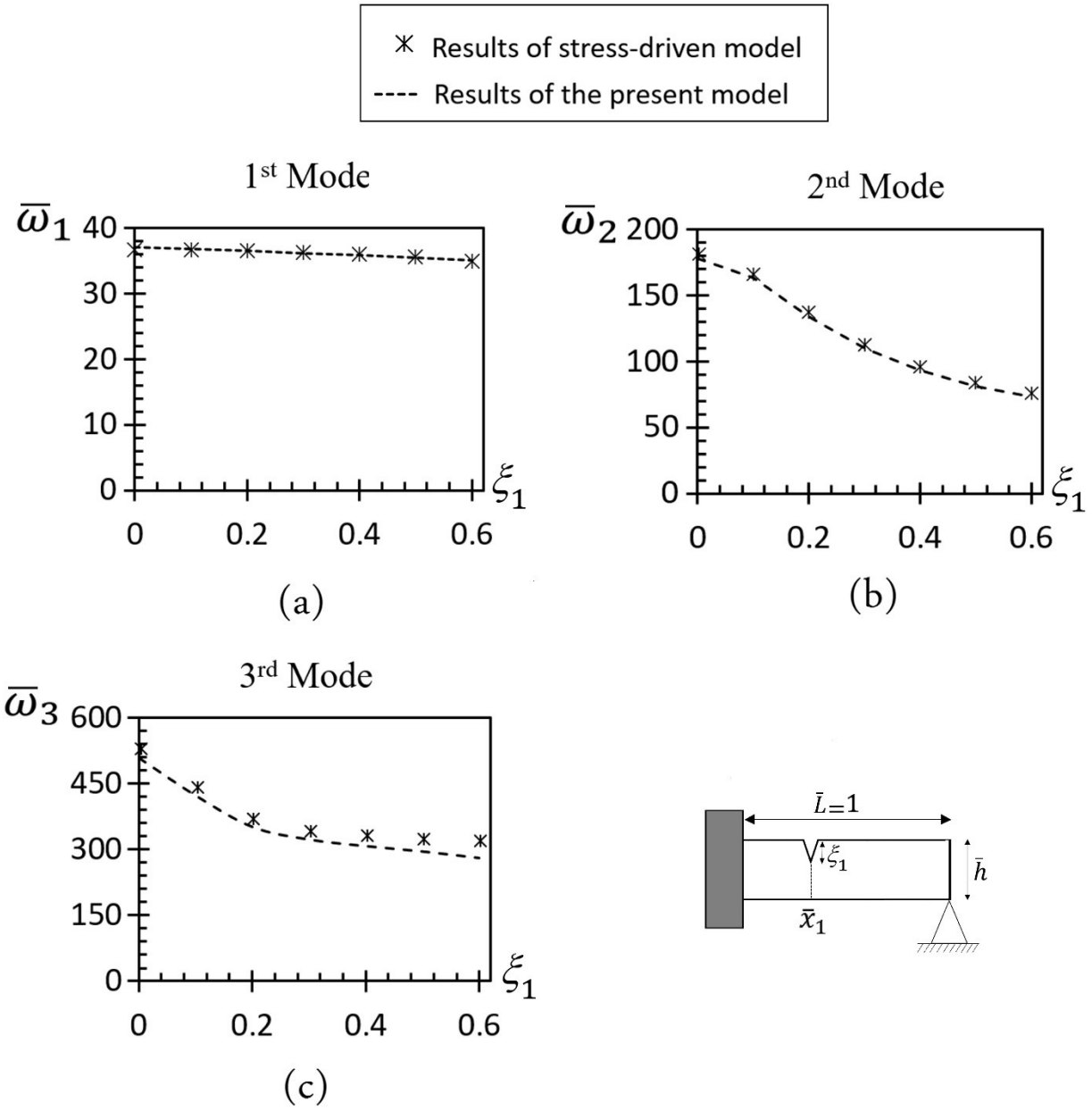

Fig. 6 The first three dimensionless natural frequencies of a Bernoulli-Euler small-scale beam with varying crack length ξ_1. The results of the SDGE model with $\beta \to \infty$ are compared with the results reported in [41] for a clamped-pinned beam including a crack located at $\bar{x}_1 = 0.3$ with $\bar{h} = 0.1$, and the dimensionless nonlocal parameters $\lambda_C = 0.5$, $\lambda_l = 0$ and $\alpha = 0$.

In Fig. 7, the first dimensionless natural frequencies derived from the stress-driven model in [41] are compared with those obtained using the present model for a Bernoulli-Euler cantilever beam

with $\bar{h} = 0.1$, containing two cracks located at $\bar{x}_1 = 0.1$ and at $\bar{x}_2 = 0.2$. The results are presented for the dimensionless nonlocal parameters $\lambda_C = 0.25$, $\lambda_l = 0$ and $\alpha = 0$, and $\beta \to \infty$.
While the length of the first crack is constant at $\xi_1 = 0.7$, the length of the second crack varies. As evident from the figure, both models predict very similar results. For the considered case, when the length of the second crack is $\xi_2 = 0.6$, the natural frequency is 11.8 % lower than that of the beam without a second crack.

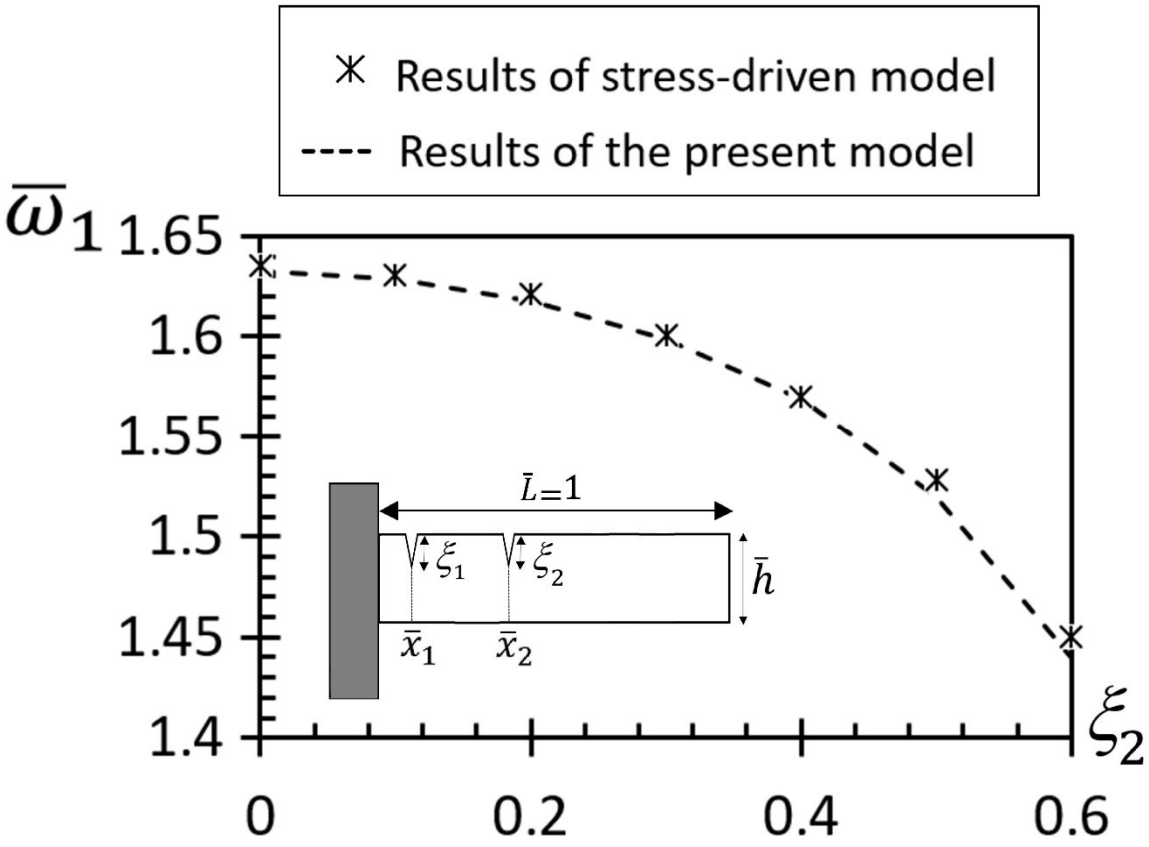

Fig. 7 First dimensionless natural frequencies of a Bernoulli-Euler small-scale beam with two cracks. The first crack is located at $\bar{x}_1 = 0.1$ with the length of $\xi_1 = 0.7$, and the second crack is located at $\bar{x}_2 = 0.2$ with varying length ξ_2. The results of SDGE model with $\beta \to \infty$ are compared with the results reported in [41] for a cantilever beam with $\bar{h} = 0.1$, and dimensionless nonlocal parameters $\lambda_C = 0.25$, $\lambda_l = 0$, $\alpha = 0$.

Additionally, the results from the stress-driven model presented by [41] are compared with those from the SDGE model, in Fig. 8, for a Bernoulli-Euler small-scale beam with $\bar{h} = 0.1$ and simply-supported boundary conditions, containing three cracks. The first and second cracks, located at

$\bar{x}_1 = 0.2$ and at $\bar{x}_2 = 0.5$, respectively, have the same length of $\xi_1 = \xi_2 = 0.4$, while the third crack at $\bar{x}_3 = 0.7$ has a varying length of ξ_3. The results are presented for the dimensionless nonlocal parameters $\lambda_C = 0.5$, $\lambda_l = 0$ and $\alpha = 0$, and $\beta \to \infty$.

It is evident from the diagram that as the length of the third crack increases, natural frequencies decrease. For the considered case, increasing the length of the third crack to $\xi_3 = 0.6$ results in a 26.6% reduction in natural frequency compared to a beam without this crack.

Finally, the accuracy of the SDGE model has been verified by comparing its results for the free transverse vibrations of large-scale Timoshenko cracked beams, showing good agreement with the results reported in [28].

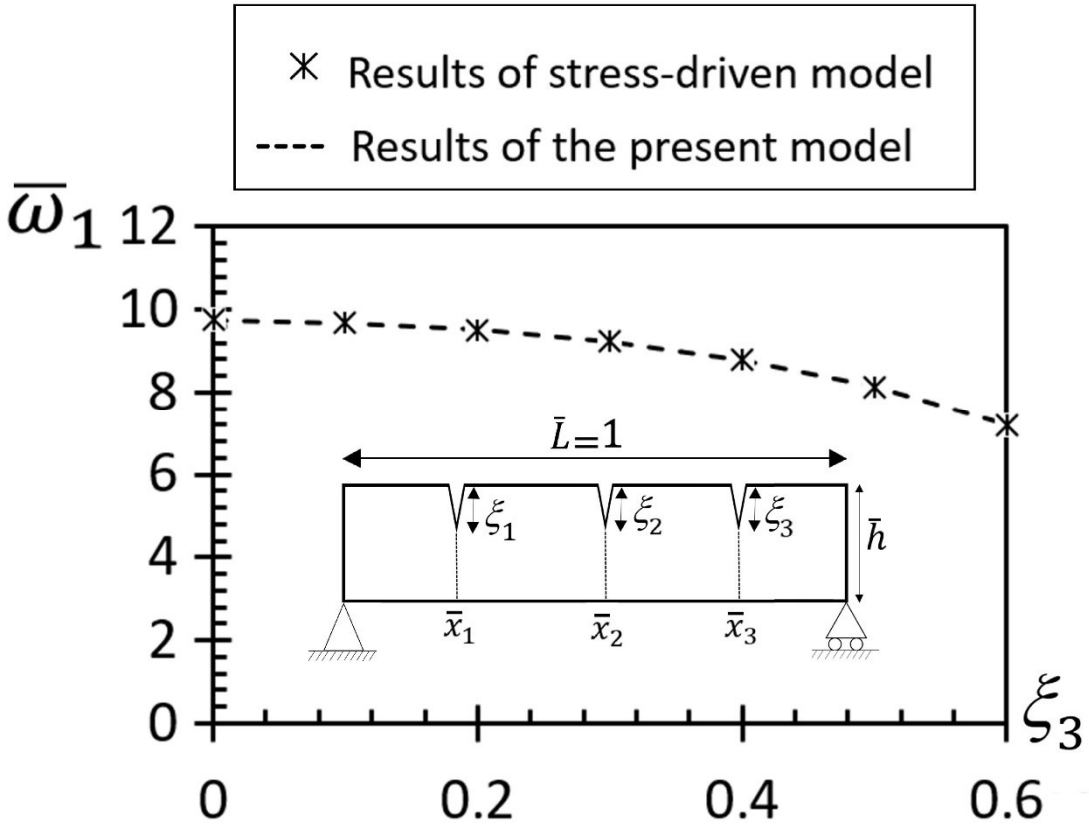

Fig. 8 First dimensionless natural frequencies of a Bernoulli-Euler small-scale beam with three cracks located at $\bar{x}_1 = 0.2$, $\bar{x}_2 = 0.5$ and $\bar{x}_3 = 0.7$. The first two cracks have a length of $\xi_1 = 0.4$ and $\xi_2 = 0.4$, while the third crack has a varying length ξ_3. The results of SDGE model with $\beta \to \infty$ are compared with those reported in [41] for a simply-supported beam with $\bar{h} = 0.1$, and dimensionless nonlocal parameters $\lambda_C = 0.5$, $\lambda_l = 0$ and $\alpha = 0$.

5.2. Effects of dimensionless shear rigidity parameter β

Fig. 9 illustrates how the Timoshenko beam theory reduces to the Bernoulli-Euler beam theory for a small-scale intact beam as the dimensionless shear rigidity β approaches infinity. The natural frequencies are normalized by calculating the ratio of the first natural frequency of the Timoshenko small-scale beam to the corresponding frequency of the Bernoulli-Euler small-scale beam denoted as $(\omega_1)_{B.E.B}$. The diagrams of normalized natural frequencies for small-scale beams under various boundary conditions show that as β increases, the natural frequencies rise and gradually approach the values predicted by the Bernoulli-Euler beam theory.

Among the four boundary conditions examined, the natural frequencies of cantilever beams are closer to those of Euler-Bernoulli beams across all sets of nonlocal parameters. For instance, with $\lambda_C = 0.5$, $\lambda_l = 0.5$, $\alpha = 0.5$ and $\beta = 16$, the frequency ratio in Fig. 9 is 0.867. In contrast, the fully-clamped beam exhibits the lowest frequency ratio equal to 0.534 for the corresponding values.

The nonlocal parameters also influence the effect of shear rigidity on the natural frequencies. For example, at $\beta = 16$, the frequency ratio for the fully-clamped miniaturized beam is 0.478 when $\lambda_C = 0.5$, $\lambda_l = 0$ and $\alpha = 0.5$ (Fig. 9(c)), showing a 10.5% reduction compared to the case with the same length scale and mixture parameters but $\lambda_l = 0.5$ (Fig. 9(a)). This suggests that decreasing the dimensionless gradient length parameter λ_l intensifies the effect of shear deformation.

Furthermore, the dimensionless length scale parameter λ_C significantly impacts the influence of shear rigidity. For instance, at $\beta = 16$, with $\lambda_C = 0$, $\lambda_l = 0.5$ and $\alpha = 0.5$ (Fig. 9(d)), the frequency ratio for the fully-clamped beam is 0.671, which is 25.65% higher than in the case where $\lambda_C = 0.5$, $\lambda_l = 0.5$, and $\alpha = 0.5$ (Fig. 9(a)). This implies that increasing the dimensionless length scale parameter λ_C increases the effect of shear deformation. The mixture parameters α has a minor effect on the change in natural frequencies with varying β as can be seen by comparing the curves in Fig. 9(a) and Fig. 9(b).

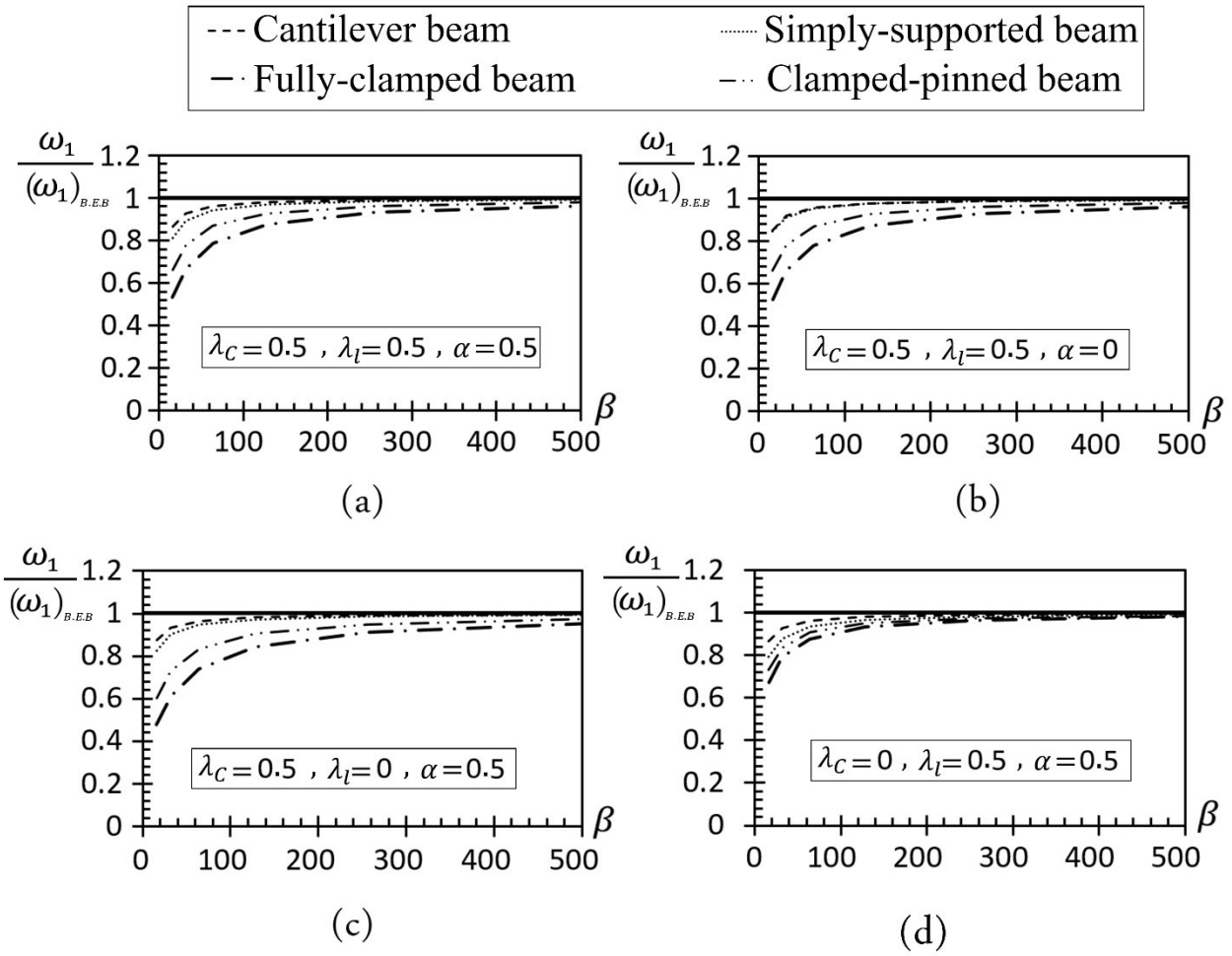

Fig. 9 Ratios of natural frequencies to those of a Bernoulli-Euler beam for a small-scale intact beam with $\bar{h} = {}^{1}/_{6}$, and varying dimensionless shear rigidity β, for different boundary conditions and dimensionless nonlocal parameters (a) $\lambda_C = 0.5$, $\lambda_l = 0.5$, $\alpha = 0.5$, (b) $\lambda_C = 0.5$, $\lambda_l = 0.5$, $\alpha = 0$, (c) $\lambda_C = 0.5$, $\lambda_l = 0$, $\alpha = 0.5$, and (d) $\lambda_C = 0$, $\lambda_l = 0.5$, $\alpha = 0.5$.

Fig. 10 shows the impact of dimensionless shear rigidity β on the variation of the first natural frequencies of a small-scale cracked beam with $\bar{h} = {}^{1}/_{6}$ as the crack length ξ_1 increases. The analysis is conducted for the dimensionless nonlocal parameters $\lambda_C = 0.75$, $\lambda_l = 0.25$ and $\alpha = 0.5$, considering four types of boundary conditions with different crack locations $\bar{x}_1$.

As can be seen, the smallest variation in natural frequencies as the crack length increases occurs for the fully-clamped small-scale beam when $\beta = 10$. The first dimensionless natural frequency without a crack is $\bar{\omega}_1 = 11.5426$, and it decreases to $\bar{\omega}_1 = 10.5515$ when a crack with a length

of $\xi_1 = 0.6$ is introduced at $\bar{x}_1 = 0.05$, representing a modest reduction of 8.6%. In contrast, the most significant variation in natural frequencies is observed for the Bernoulli-Euler cantilever small-scale beam ($\beta \to \infty$). In this case, the first dimensionless natural frequency drops from $\bar{\omega}_1 = 4.2730$ for the intact beam to $\bar{\omega}_1 = 2.0587$ when a crack with a length of $\xi_1 = 0.6$ is located at $\bar{x}_1 = 0.2$, resulting in a substantial decrease of 51.82%.

Additionally, as the crack length increases, the curves for different values of dimensionless shear rigidity β gets closer to each other in all cases. This suggests that the shear rigidity has a lower influence on the natural frequencies as the crack length increases.

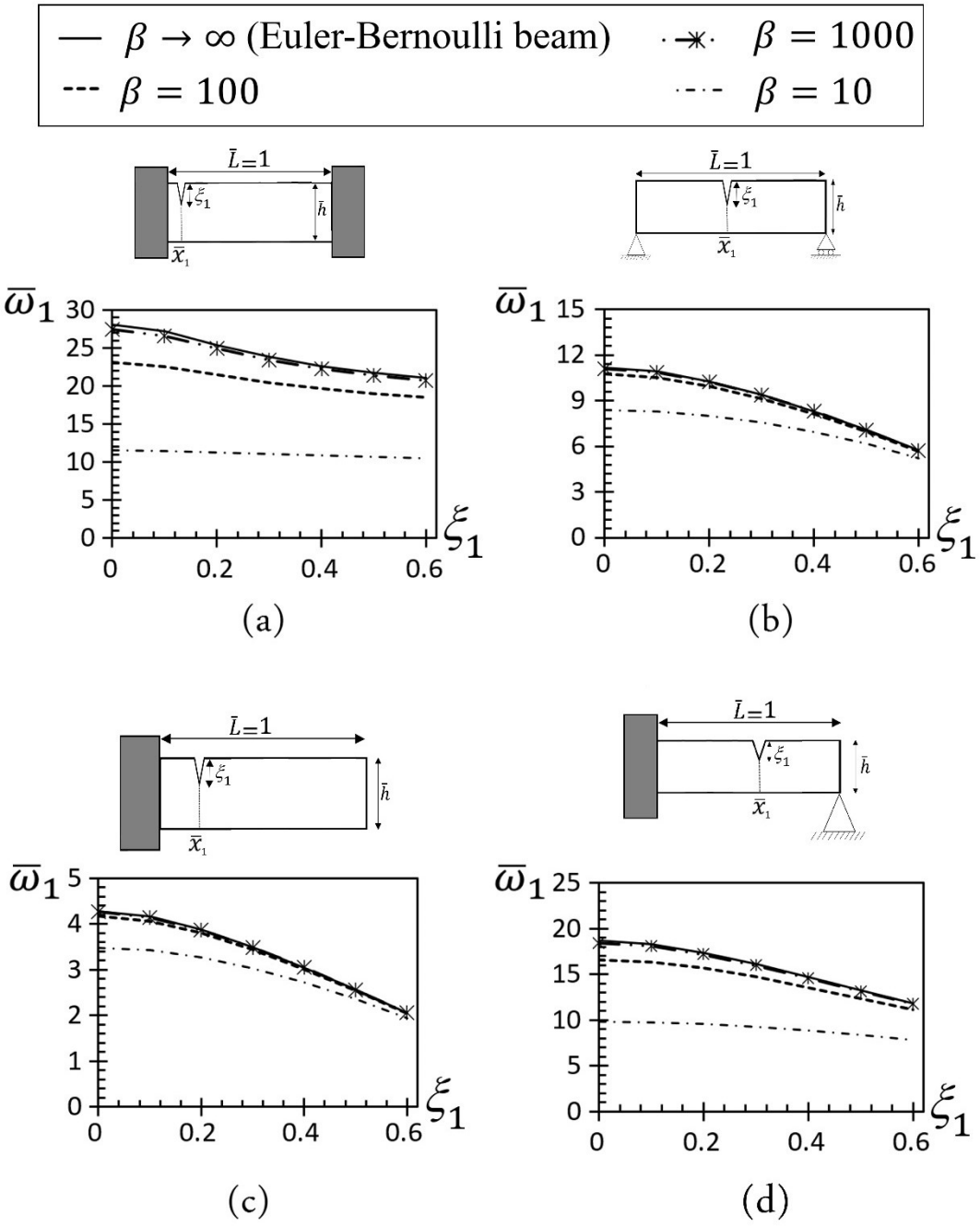

Fig. 10 First dimensionless natural frequencies of a small-scale cracked beam with $\bar{h} = {}^{1}/_{6}$, and varying crack length ξ_1. The results are presented for dimensionless nonlocal parameters $\lambda_C = 0.75$, $\lambda_l = 0.25$, $\alpha = 0.5$, and different values of dimensionless shear rigidity β for (a) a fully-clamped beam with a crack located at $\bar{x}_1 = 0.05$, (b) a simply-supported beam with a crack located at $\bar{x}_1 = 0.5$, (c) a cantilever beam with a crack located at $\bar{x}_1 = 0.2$, and (d) a clamped-pinned beam with a crack located at $\bar{x}_1 = 0.6$.

5.3. Effects of length and location of crack

The effects of location and length of crack on the first three natural frequencies of a miniaturized Timoshenko beam with cantilever and simply-supported boundary conditions are illustrated in Fig. 11 and Fig. 12, respectively, for the dimensionless nonlocal parameters $\lambda_C = 0.5$, $\lambda_l = 0.5$ and $\alpha = 0.5$. The small-scale beam has a Poisson's ratio of $\nu = 0.3$, and a height-to-length ratio of $\bar{h} = 0.1$. Based on these values, the dimensionless shear rigidity is calculated as $\beta = 385$.

For the first mode, the dimensionless natural frequency of an intact micro- and nanocantilever beam is $\bar{\omega}_1 = 3.8851$. However, this value decreases when a crack is present in the beam, and depending on the location and length of the crack, this reduction can be significant. As shown in Fig. 11(a), the minimum value of the first natural frequencies for a small-scale cantilever beam, when the crack is positioned at $\bar{x}_1 \in \{0.1, 0.2, \dots, 0.9\}$, occurs at $\bar{x}_1 = 0.1$ with a crack length of $\xi_1 = 0.6$. This frequency, $\bar{\omega}_1 = 2.1361$, is 45% lower than that of the intact beam. This notable reduction is due to the significantly higher bending moment near the clamped end in a cantilever beam during the first mode of vibration, as illustrated in Fig. 11(b). This figure shows the distribution of dimensionless bending moments along the longitudinal direction of the intact miniaturized beam for the first vibration mode.

For the second mode, the value of the dimensionless bending moment for the intact miniaturized cantilever beam is relatively high at $\bar{x}_1 = 0.6$, as shown in Fig. 11(d). As a result, the second natural frequency of the small-scale beam with a crack at $\bar{x}_1 = 0.6$ is at its lowest compared to other positions. For a crack length of $\xi_1 = 0.6$ this value is $\bar{\omega}_2 = 13.7234$ which is 20.6% lower than the corresponding value for the intact beam.

As Fig. 11(e) shows, the third dimensionless natural frequency of the miniaturized cantilever beam without a crack is $\bar{\omega}_3 = 47.6882$. When a crack is present, the minimum value is $\bar{\omega}_3 = 35.9963$, which is 24.5% lower than that of the intact beam. This frequency is observed when the crack is located at $\bar{x}_1 = 0.7$ with a length of $\xi_1 = 0.6$.

Looking at Fig. 12, it is clear that for the simply-supported boundary conditions, there is symmetry in all natural frequencies with respect to the midspan of the beam. This symmetry arises from the symmetric bending moment distribution along the length of the simply-supported intact micro- and nanobeam.

As shown in Fig. 12(b), for the first mode, the bending moment reaches its maximum at $\bar{x}_1 = 0.5$. Consequently, the first natural frequency significantly decreases at this point, dropping from $\bar{\omega}_1 = 8.7340$ for an intact beam to $\bar{\omega}_1 = 6.1718$ for a beam with a crack length of $\xi_1 = 0.6$.

In Fig. 12(d), it is observed that for the second mode, the bending moment is maximum at $\bar{x}_1 = 0.25$ and $\bar{x}_1 = 0.75$. As a result, the second natural frequency is minimized when a crack is located at any of these locations. For a small-scale simply-supported beam with a crack length of $\xi_1 = 0.6$, the second dimensionless natural frequency is $\bar{\omega}_2 = 25.0351$, indicating a 19.7% reduction compared to the $\bar{\omega}_2 = 31.1918$ obtained for an intact beam.

For the third mode of free transverse vibration, as Fig. 12(e) illustrates, the dimensionless natural frequency for the small-scale beam without a crack is $\bar{\omega}_3 = 64.9443$. However, in the presence of a single crack, it decreases, reaching a minimum value of $\bar{\omega}_3 = 53.6756$ when the crack is located at $\bar{x}_1 = 0.1$ and $\bar{x}_1 = 0.9$ with a crack length of $\xi_1 = 0.6$.

The insights gained in this section about the effects of crack length and location on frequencies align with the findings reported in [41].

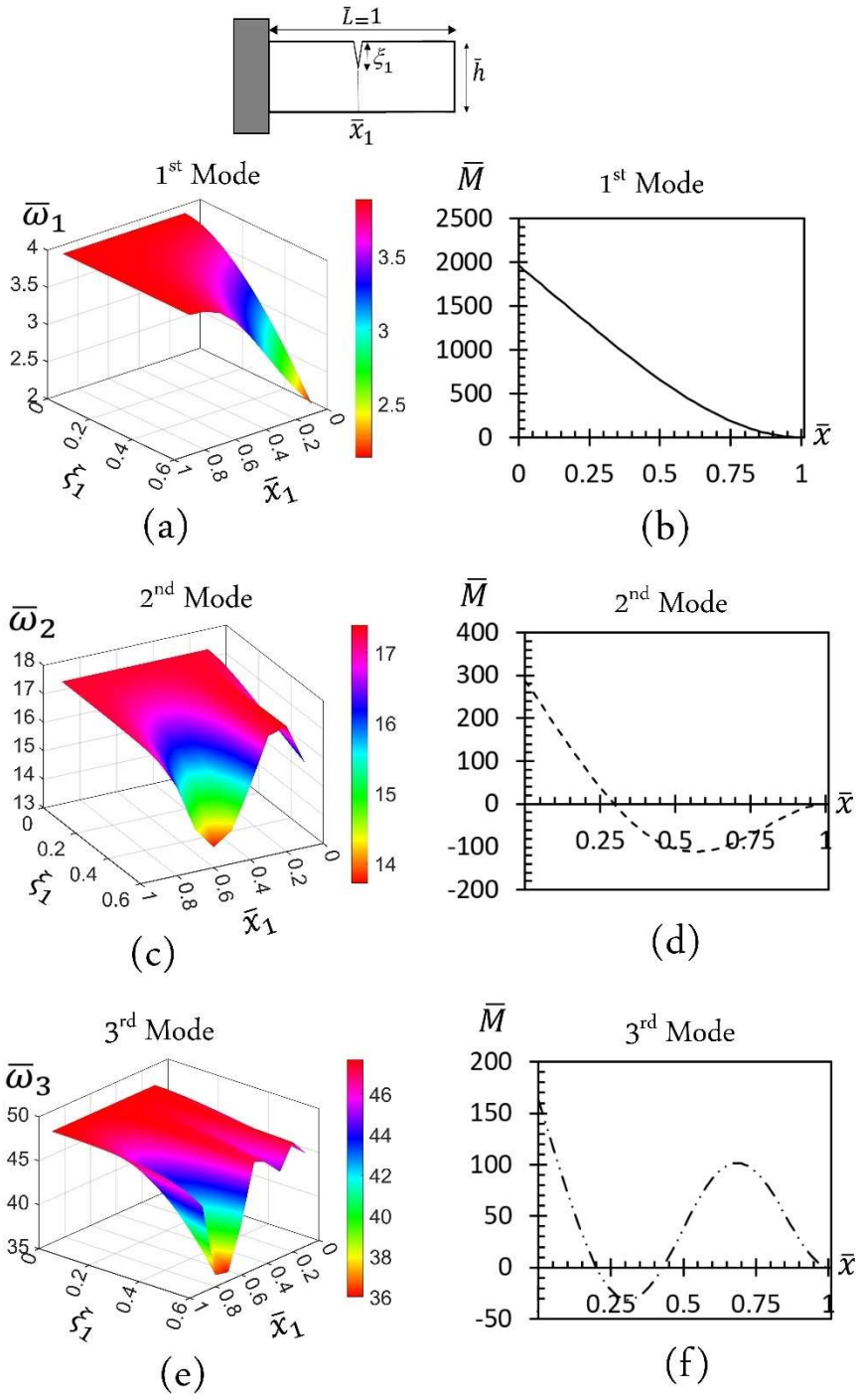

Fig. 11 First three dimensionless natural frequencies of a Timoshenko small-scale cantilever beam with $\nu = 0.3$, $\bar{h} = 0.1$ and $\beta = 385$ as a function of crack length ξ_1 and crack location $\bar{x}_1$ for the (a) first mode, (c) second mode, (e) third mode. The dimensionless bending moments along the length of the miniaturized beam, without a crack, are shown in (b), (d), and (f), respectively. The results are presented for the dimensionless nonlocal parameters $\lambda_C = 0.5$, $\lambda_l = 0.5$ and $\alpha = 0.5$.

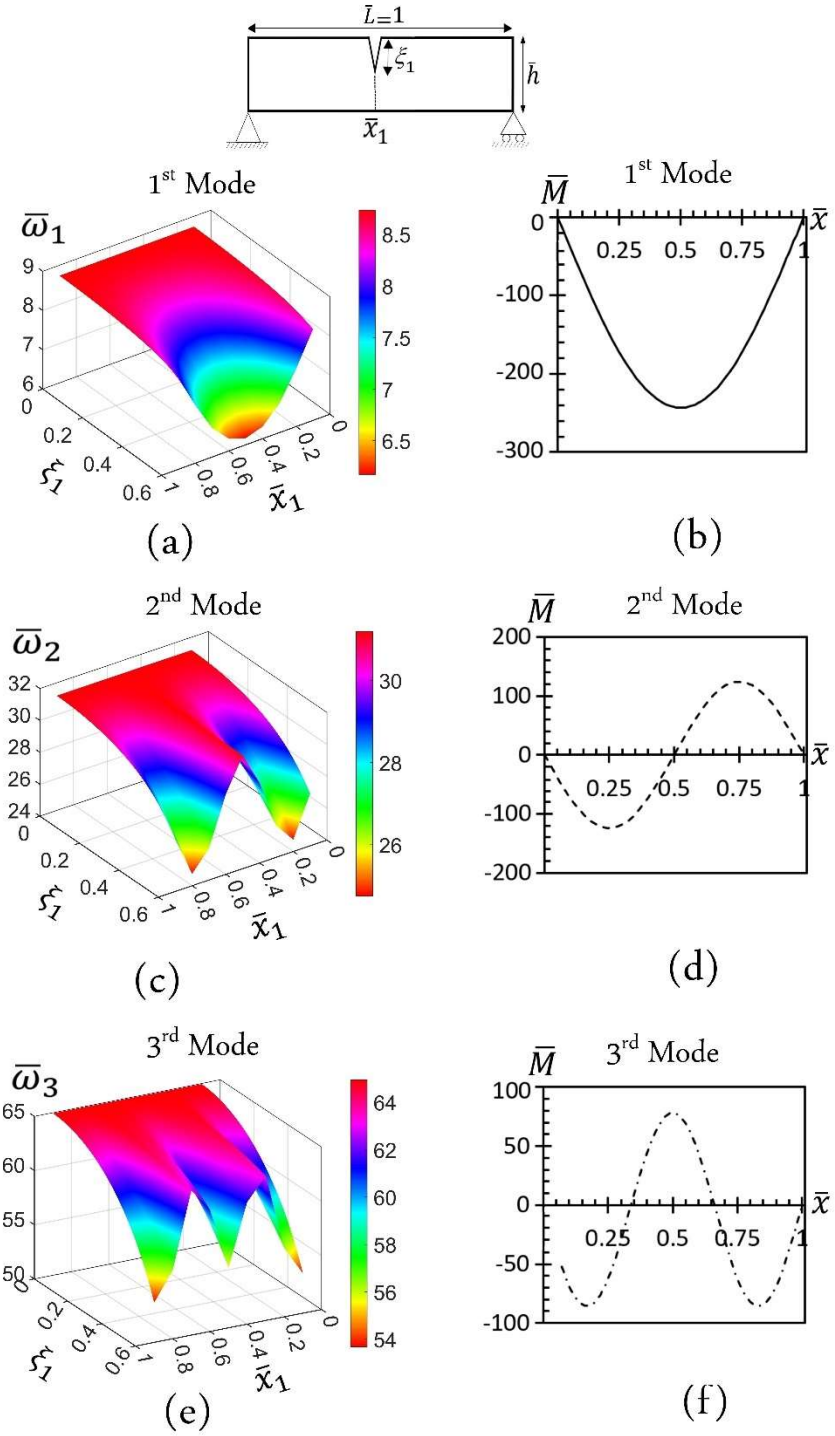

Fig. 12 First three dimensionless natural frequencies of a Timoshenko small-scale simply-supported beam with $\nu = 0.3$, $\bar{h} = 0.1$ and $\beta = 385$ as a function of crack length ξ_1 and crack location $\bar{x}_1$ for the (a) first mode, (c) second mode, (e) third mode. The dimensionless bending moments along the length of the miniaturized beam, without a crack, are shown in (b), (d), and (f), respectively. The results are presented for the dimensionless nonlocal parameters $\lambda_C = 0.5$, $\lambda_l = 0.5$ and $\alpha = 0.5$.

5.4. Effects of nonlocal parameters

The effects of nonlocal parameters on the free transverse vibrations of small-scale Timoshenko beam including a crack located at the midspan with the length of $\xi_1 = 0.5$, are illustrated in Fig. 13. The miniaturized beam has a height-to-length ratio of $\bar{h} = 0.1$ and the dimensionless shear rigidity $\beta = 385$. The results are presented for the fully-clamped and clamped-pinned boundary conditions.

In general, it is clear that increasing the dimensionless length scale parameter λ_C leads to higher natural frequencies for both fully-clamped and clamped-pinned beams. This is because a higher λ_C makes the small-scale beam stiffer, resulting in increased natural frequencies. For instance, for the fully-clamped cracked beam with $\lambda_l = 0.6$, $\alpha = 0$, and $\lambda_C = 0.2$, the first dimensionless natural frequency is $\bar{\omega}_1 = 11.4023$. When λ_C is increased to 0.8, the frequency increases to $\bar{\omega}_1 = 32.2089$, representing a significant increase of 182.5 %. Similarly, for the clamped-pinned beam, the corresponding values are 7.5105 and 17.5494, respectively, which indicates a rise of 133.7 %. On the other hand, an increase in the dimensionless gradient length parameter λ_l results in a reduction of natural frequencies, demonstrating a softening behavior. For example, the first dimensionless natural frequency of the fully-clamped cracked beam with $\lambda_C = 0.2$, $\alpha = 0$, and $\lambda_l = 0.2$ is $\bar{\omega}_1 = 22.2849$. When λ_l is increased to 0.6, the frequency decreases by 48.8 %, falling to $\bar{\omega}_1 = 11.4023$. Similarly, for the clamped-pinned beam, the corresponding values are 14.5617 and 7.5105, respectively, indicating a decrease of 48.4 %.

Additionally, the mixture parameter, which controls the nonlocality in the SDGE model, affects the natural frequencies, particularly when λ_C has high values. Increasing α further lowers the natural frequencies by intensifying the local contribution to the model. For example, in the case of a fully-clamped beam, the ratio of the first natural frequency with dimensionless nonlocal parameters $\lambda_C = 0.2$, $\lambda_l = 0.8$ and $\alpha = 0.5$, to that with $\lambda_C = 0.2$, $\lambda_l = 0.8$ and $\alpha = 0$ is 0.94. However, when the dimensionless length scale parameter λ_C is increased to 0.8, the ratio of the first natural frequency with $\alpha = 0.5$ and $\lambda_l = 0.8$, to that with $\alpha = 0$ and $\lambda_l = 0.8$ decreases significantly to 0.65. For clamped-pinned boundary conditions, the ratio between the first natural frequency with dimensionless nonlocal parameters $\lambda_C = 0.2$, $\lambda_l = 0.8$ and $\alpha = 0.5$ and that with $\lambda_C = 0.2$, $\lambda_l = 0.8$ and $\alpha = 0$ is 0.98. When the dimensionless length scale parameter λ_C is increased to 0.8, the ratio of the first natural frequency with $\alpha = 0.5$ and $\lambda_l = 0.8$, to that with $\alpha = 0$ and $\lambda_l = 0.8$ reduces to 0.81.

Based on the comparisons made for each of the parameters λ_C, λ_l and α, it can be concluded that the type of boundary conditions also affects the impact of the nonlocal parameters on the frequencies.

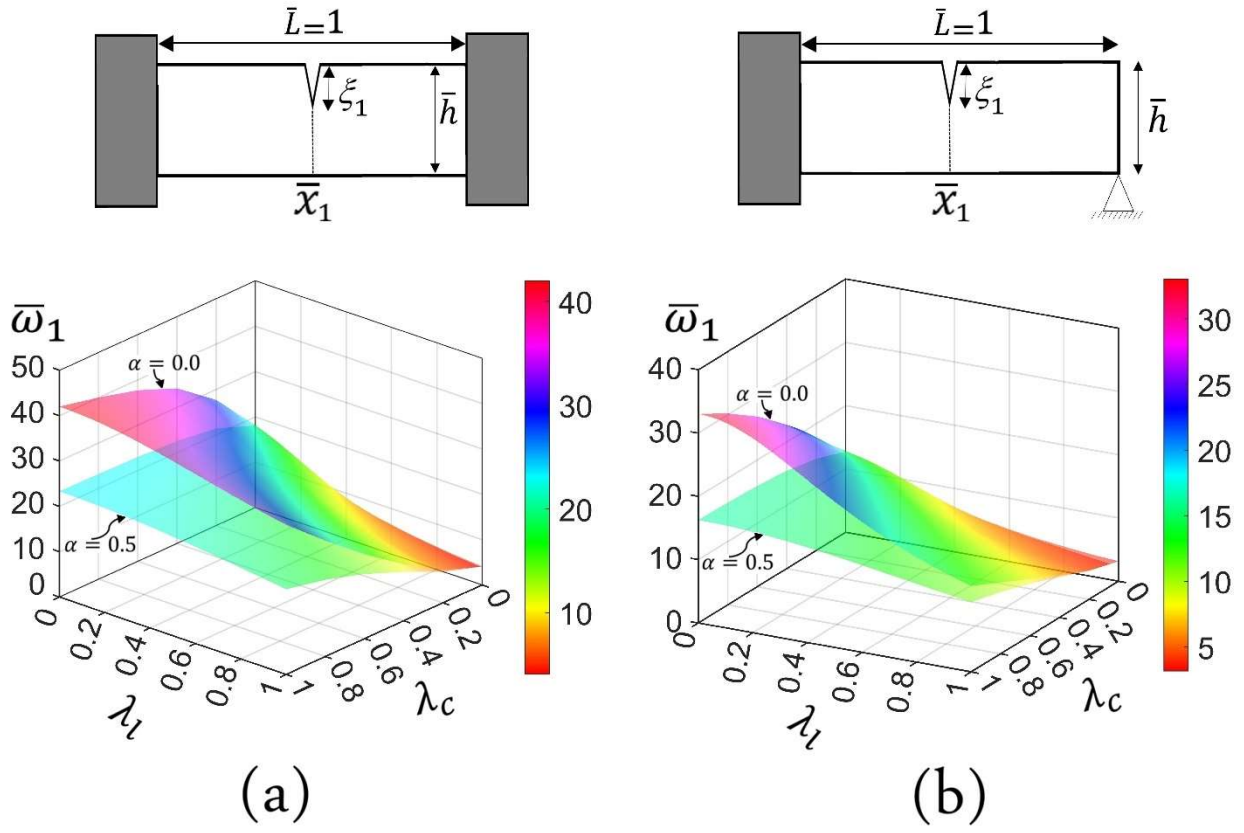

Fig. 13 First dimensionless natural frequencies of a small-scale Timoshenko beam with variations in the dimensionless nonlocal parameters λ_C, λ_l and α The results are presented for (a) fully-clamped beam, (b) clamped-pinned beam with $\nu = 0.3, \bar{h} = 0.1$ and $\beta = 385$, including a crack with the length of $\xi_1 = 0.5$ located at $\bar{x}_1 = 0.5$.

5.5. Effects of multiple cracks

The developed SDGE model can be readily applied to study the free transverse vibration of miniaturized beams with an arbitrary number of cracks. In this section, the impact of two and three cracks on the first natural frequencies of small-scale beams is examined.

Fig. 14 illustrates how the first natural frequencies of a small-scale Timoshenko beam with $\bar{h} = 0.1$ and $\beta = 385$ vary under fully-clamped and clamped-pinned boundary conditions as the length

of the second crack at $\bar{x}_2 = 0.4$ increase. The first crack is fixed at $\bar{x}_1 = 0.2$ with a constant length of $\xi_1 = 0.5$.

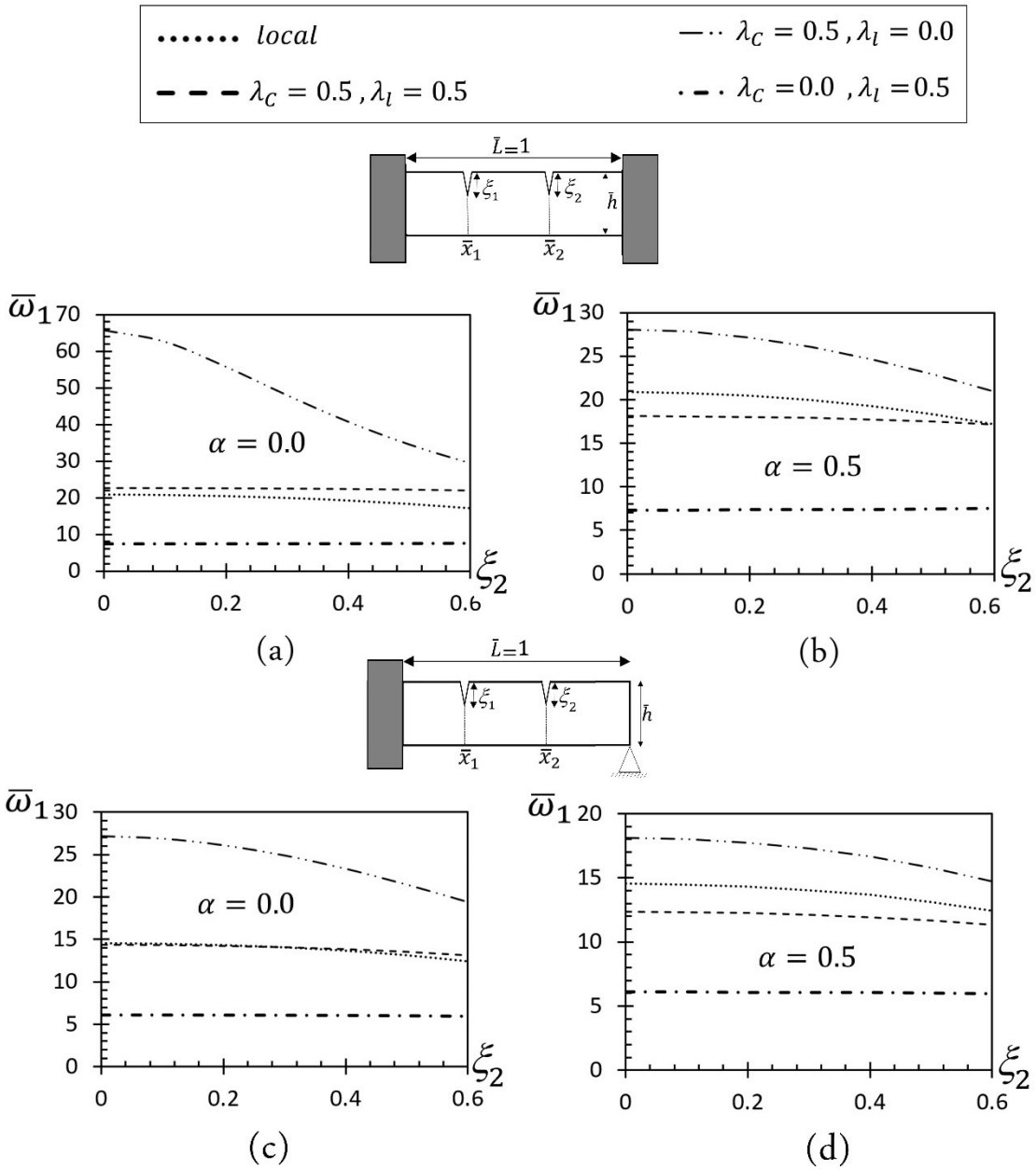

Fig. 14 First dimensionless natural frequencies of a Timoshenko small-scale beam with two cracks at $\bar{x}_1 = 0.2$ with the crack length of $\xi_1 = 0.5$, and at $\bar{x}_2 = 0.4$ with varying crack length ξ_2. The results are presented for (a), (b) fully-clamped, and (c), (d) clamped-pinned beam, with $\nu = 0.3, \bar{h} = 0.1$ and $\beta = 385$.

In general, the values of the nonlocal parameters have a significant impact on how the increasing length of the second crack affects the natural frequencies. For both fully-clamped and clamped-pinned boundary conditions, the variation in natural frequencies is more notable when the dimensionless nonlocal parameters are $\lambda_C = 0.5$, $\lambda_l = 0$ and $\alpha = 0$. This indicates that for these nonlocal parameters, the natural frequencies of the small-scale beam are highly dependent on the length of the second crack. For the fully-clamped beam with the abovementioned nonlocal parameters, the first dimensionless natural frequency is $\bar{\omega}_1 = 65.7652$ when only the first crack is present. However, with the addition of the second crack with a length of $\xi_2 = 0.6$, the frequency decreases to $\bar{\omega}_1 = 29.4001$, representing a 55.3% reduction. In the case of the clamped-pinned beam, the decrease is 28.6% with the frequency dropping from $\bar{\omega}_1 = 27.1545$ for the beam with only the first crack to $\bar{\omega}_1 = 19.3798$ when the second crack with a length of $\xi_2 = 0.6$ is introduced.

Additionally, as the mixture parameter α increases to 0.5, the variation in natural frequencies for the case with $\lambda_C = 0.5$ and $\lambda_l = 0$ is still highlighted compared to other cases with different nonlocal parameters. However, the decrease in in natural frequencies is less significant than in the case where $\lambda_C = 0.5$, $\lambda_l = 0$ and $\alpha = 0$ for both fully-clamped and clamped-pinned boundary conditions.

In other cases, the second crack has a weaker effect on the natural frequencies. For a fully-clamped local beam, introducing a second crack reduces the natural frequency from $\bar{\omega}_1 = 20.8574$ for a beam with only the first crack to $\bar{\omega}_1 = 17.1954$ when a second crack with the length of $\xi_2 = 0.6$ is present, indicating a reduction of 17.6 %. For a local beam with clamped-pinned boundary conditions, the natural frequencies decrease from 14.5360 to 12.4215, representing a reduction of 14.5 %. For all cases with $\lambda_C = 0.5$ and $\lambda_l = 0.5$, as shown in Fig. 14, the second crack has a negligible impact on the natural frequencies for both fully-clamped and clamped-pinned boundary conditions, with only slight variation observed as the crack length changes.

Fig. 15 illustrates the variations in the first natural frequencies of a small-scale beam with $\bar{h} = 0.1$ and $\beta = 385$, containing three cracks. The first crack is located at $\bar{x}_1 = 0.25$ and has a varying length ξ_1, while the second and third cracks are positioned at $\bar{x}_2 = 0.5$ and $\bar{x}_3 = 0.75$, respectively, each with the fixed lengths of $\xi_2 = \xi_3 = 0.5$.

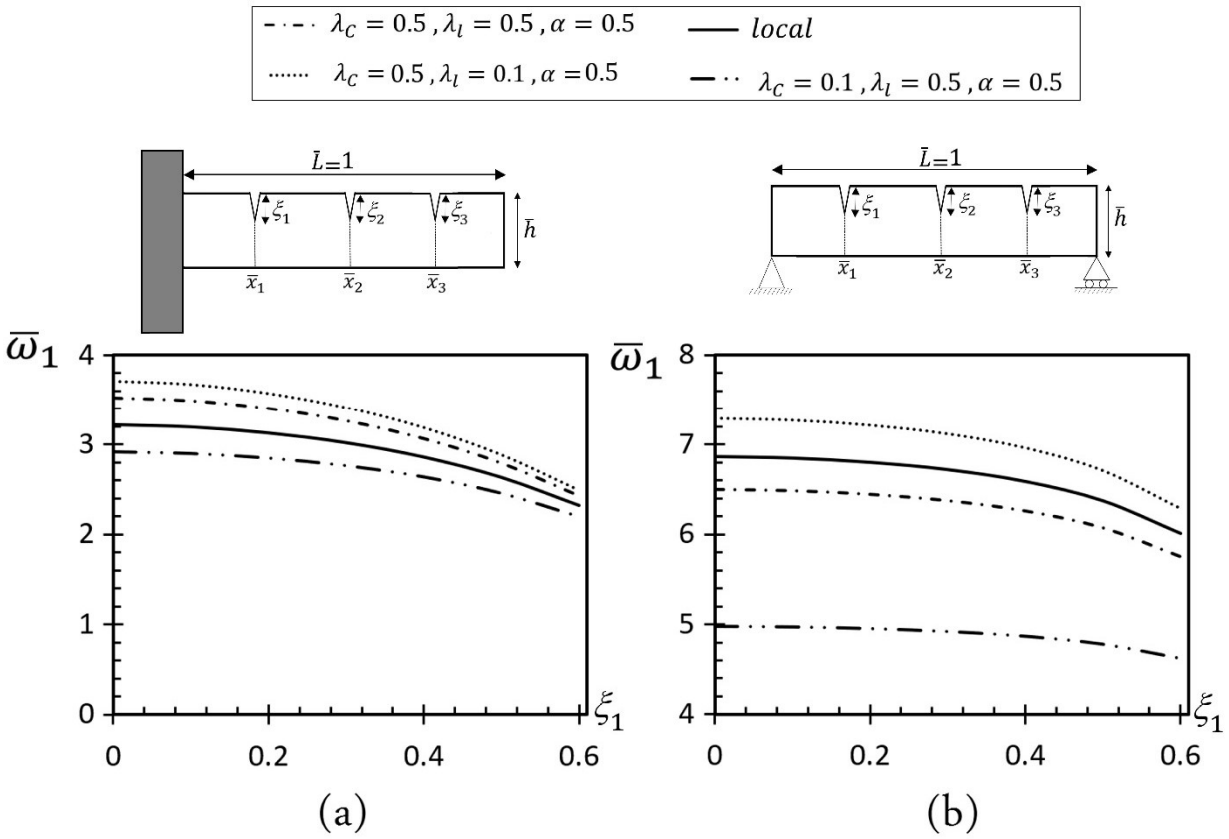

Fig. 15 First dimensionless natural frequencies of a Timoshenko small-scale beam with $\nu = 0.3, \bar{h} = 0.1$ and $\beta = 385$, containing three cracks located at $\bar{x}_1 = 0.25$, $\bar{x}_2 = 0.5$ and $\bar{x}_3 = 0.75$. The first crack has a varying length of ξ_1, while the length of the second and third cracks are $\xi_2 = \xi_3 = 0.5$. The results are presented for (a) cantilever beam, and (b) simply-supported beam.

For a small-scale intact cantilever beam, the bending moment at $\bar{x}_1$, located near the clamped end, is high, causing the crack at this position to significantly impact the natural frequencies. When the dimensionless nonlocal parameters are set to $\lambda_C = 0.5$, $\lambda_l = 0.1$ and $\alpha = 0.5$, the natural frequencies are higher compared to other scenarios. Additionally, the variation in natural frequencies becomes more pronounced as the length of the first crack increases under these parameters. For example, with $\lambda_C = 0.5$, $\lambda_l = 0.1$ and $\alpha = 0.5$, the natural frequency decreases from $\bar{\omega}_1 = 3.7076$, in the absence of the first crack, to $\bar{\omega}_1 = 2.4892$ when the first crack has a length of $\xi_1 = 0.6$, representing a reduction of 32.9%. The corresponding decreases due to introducing the first crack with a length of $\xi_1 = 0.6$ are 32.7% for the case with dimensionless

nonlocal parameters $\lambda_C = 0.5$, $\lambda_l = 0.5$, $\alpha = 0.5$, and 24.7 % for the case with $\lambda_C = 0.1$, $\lambda_l = 0.5$, $\alpha = 0.5$. Additionally, for a local beam, this reduction is 27.9%.

For the simply-supported beam, the impact of the first crack on the natural frequencies is notably less compared to the cantilever beam. This is due to the relatively low bending moment at $\bar{x}_1 = 0.25$ for the simply-supported beam. In the case with dimensionless nonlocal parameters $\lambda_C = 0.5$, $\lambda_l = 0.1$ and $\alpha = 0.5$, the natural frequency decreases by 13.8% due to the introduction of the first crack with a length of $\xi_1 = 0.6$. The corresponding reductions for a local beam and small-scale beams with dimensionless nonlocal parameters $\lambda_C = 0.5$, $\lambda_l = 0.5$, $\alpha = 0.5$ and $\lambda_C = 0.1$, $\lambda_l = 0.5$, $\alpha = 0.5$ are 12.5 %, 11.4 %, and 7.2 % respectively.

The first three mode shapes for the free transverse vibration of a Timoshenko cantilever beam with three equally spaced cracks, each with a length of $\xi_1 = \xi_2 = \xi_3 = 0.5$, are shown in Fig. 16. As observed, the mode shapes change with varying values of the nonlocal parameters, with these differences being more highlighted in the second and third modes. Consequently, the locations of maximum deflection along the beam experience slight shifts.

Moreover, as shown in Fig. 16(a), for the first mode of vibration in all cases, the first crack at $\bar{x}_1 = 0.25$ has the most significant effect on the mode shape. In the second mode, the second crack at $\bar{x}_2 = 0.5$ has a more considerable influence on the mode shape. For the third mode, both the first crack at $\bar{x}_1 = 0.25$ and third crack at $\bar{x}_3 = 0.75$ have the most notable impact on the mode shape.

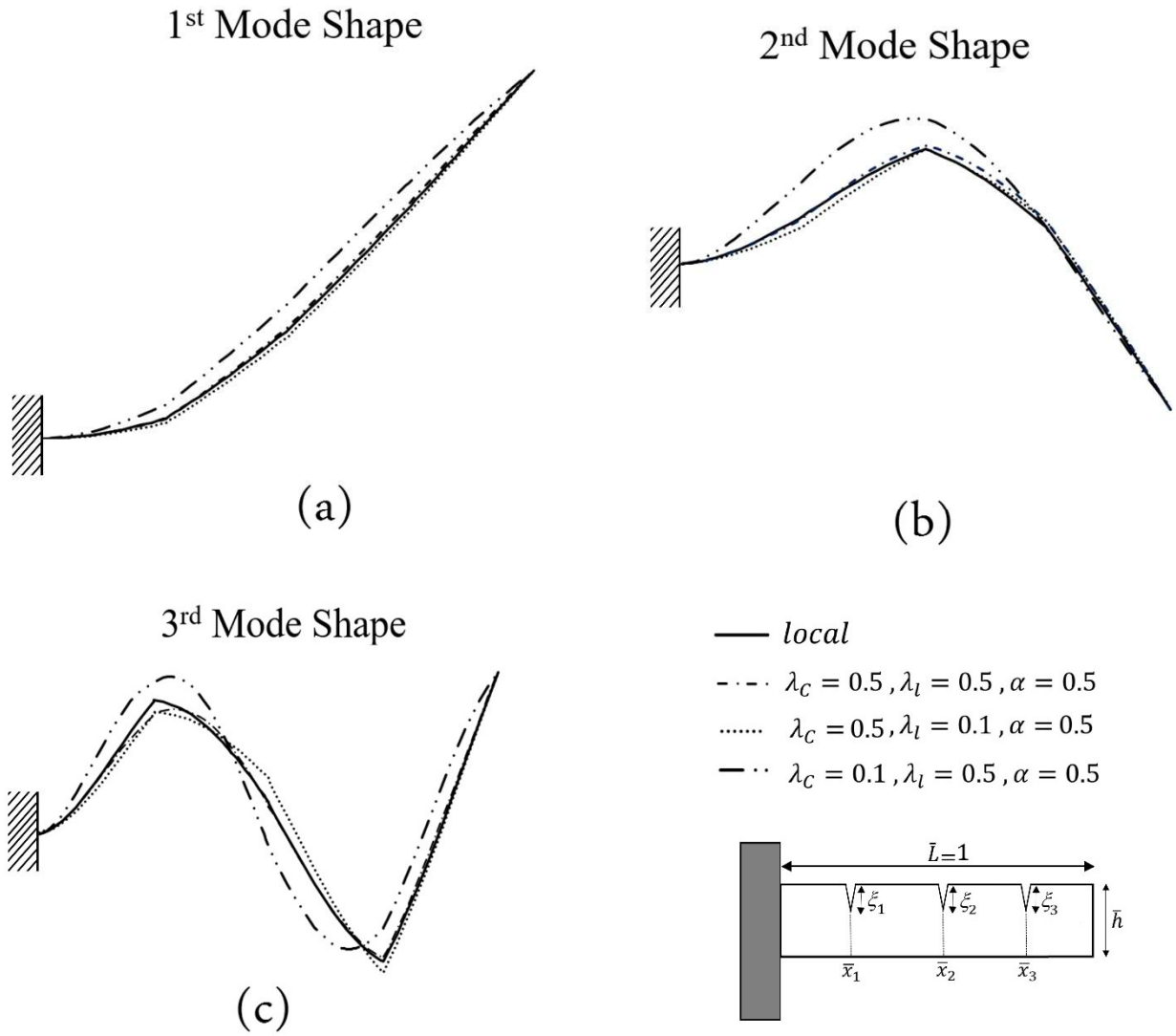

Fig. 16 The first three mode shapes of a Timoshenko small-scale cantilever beam with $\nu = 0.3, \bar{h} = 0.1$ and $\beta = 385$, containing three cracks located at $\bar{x}_1 = 0.25$, $\bar{x}_2 = 0.5$ and $\bar{x}_3 = 0.75$. The lengths of all cracks are equal, with $\xi_1 = \xi_2 = \xi_3 = 0.5$.

6. Conclusions

We have investigated the size-dependent free transverse vibration of small-scale cracked Timoshenko beams. The effect of cracks on the vibration behavior is modeled by treating the sub-beams between cracks as being connected by rotational and translational springs. Size-dependence is incorporated using the integral form of the constitutive equations from the local/nonlocal stress-driven gradient elasticity (SDGE) model. Since these integral constitutive equations apply over the

entire beam, they are first converted into a set of differential constitutive equations, applicable to each sub-beam and subjected to a set of non-standard constitutive boundary and continuity conditions. The differential constitutive equations are then used to reformulate the equations of motion in terms of displacement functions. These equations are decoupled and solved, and both standard variationally consistent and non-standard constitutive boundary and continuity conditions are imposed to construct the eigenvalue problem. The natural frequencies and mode shapes, including higher-order modes, are determined by numerically solving the eigenvalue problem.

We have provided several verifications for the formulated model by comparing its predictions with experimental, molecular dynamics, and theoretical results available in the literature. In all cases, the predictions of the model are in agreement with those in the literature. The formulated model was then applied to study the effect of different parameters on the natural frequencies and mode shapes of small-scale cracked beams. First, it was shown that the effect of shear deformation on the natural frequencies depends on the nonlocal parameters and the presence of the crack. Generally, the effect of shear deformation is more pronounced in small-scale intact beams than in those with cracks. The results confirm the expected small-scale effect of the nonlocal parameters of the SDGE model, even for cracked beams: higher values of the length scale parameter and lower values of the mixture and gradient parameters increase the frequencies. As noted in previous studies, the crack has the greatest effect on natural frequencies when located at a cross-section with a high bending moment.

Funding

The financial support provided by the National Science Centre (NCN) in Poland through the grant agreement No: UMO-2022/47/D/ST8/01348, is gratefully acknowledged.

Declaration of interests

The authors declare that they have no known competing financial interests or personal relationships that could have appeared to influence the work reported in this paper.

Appendix A

To calculate the crack compliances, linear elastic fracture mechanics (LEFM) was employed. A widely-used method, introduced by [37], applies to rectangular beams with edge cracks under

plane stress conditions and subjected to both bending moment and shear force. This method yields the following expressions for the crack compliances:

$$C_M = 12\,C\,h\int_0^{\xi} F_M^2(\xi)\,d\xi \qquad for \quad 0 \le \xi \le 0.6$$

$$F_M(\xi) = \sqrt{\tan\frac{\pi\xi}{2}}\left(\frac{0.923 + 0.199(1-\sin\frac{\pi\xi}{2})^4}{\cos\frac{\pi\xi}{2}}\right) \tag{A1}$$

$$C_M = 2.6535\,C\,h\int_0^{\xi}\frac{1}{(1-\xi)^3}\,d\xi \qquad for \quad 0.6 \le \xi \le 1$$

$$C_Q = \frac{1}{6}Ch^3\int_0^{\xi}\frac{1}{1-\xi}F_Q^2(\xi)\,d\xi \qquad for \quad 0 \le \xi \le 1 \tag{A2}$$

$$F_Q(\xi) = 1.993\,\xi + 4.513\,\xi^2 - 9.516\,\xi^3 + 4.482\,\xi^4$$

where the dimensionless parameter ξ is defined as the ratio of the crack length to the height of the beam, $\xi = a/h$.

References

[1] B. Bhushan, Introduction to Nanotechnology, in: B. Bhushan (Ed.), Springer Handbook of Nanotechnology, Springer, Berlin, Heidelberg, 2017: pp. 1–19. https://doi.org/10.1007/978-3-662-54357-3_1.

[2] B. Bhushan, Nanotribology and nanomechanics of MEMS/NEMS and BioMEMS/BioNEMS materials and devices, Microelectronic Engineering 84 (2007) 387–412. https://doi.org/10.1016/j.mee.2006.10.059.

[3] V.S. Chandel, G. Wang, M. Talha, Advances in modelling and analysis of nano structures: a review, Nanotechnology Reviews 9 (2020) 230–258. https://doi.org/10.1515/ntrev-2020-0020.

[4] K.L. Ekinci, M.L. Roukes, Nanoelectromechanical systems, Review of Scientific Instruments 76 (2005) 061101. https://doi.org/10.1063/1.1927327.

[5] N.V. Lavrik, M.J. Sepaniak, P.G. Datskos, Cantilever transducers as a platform for chemical and biological sensors, Review of Scientific Instruments 75 (2004) 2229–2253. https://doi.org/10.1063/1.1763252.

[6] C.W. Lim, G. Zhang, J.N. Reddy, A higher-order nonlocal elasticity and strain gradient theory and its applications in wave propagation, Journal of the Mechanics and Physics of Solids 78 (2015) 298–313. https://doi.org/10.1016/j.jmps.2015.02.001.

[7] J.N. Reddy, Nonlocal theories for bending, buckling and vibration of beams, International Journal of Engineering Science 45 (2007) 288–307. https://doi.org/10.1016/j.ijengsci.2007.04.004.

[8] L. Tong, Y. Yu, W. Hu, Y. Shi, C. Xu, On wave propagation characteristics in fluid saturated porous materials by a nonlocal Biot theory, Journal of Sound and Vibration 379 (2016) 106–118. https://doi.org/10.1016/j.jsv.2016.05.042.

[9] N. Challamel, S. El-Borgi, M. Trabelssi, J.N. Reddy, Free vibration response of micromorphic Timoshenko beams, Journal of Sound and Vibration 591 (2024) 118602. https://doi.org/10.1016/j.jsv.2024.118602.

[10] S.C. Pradhan, J.K. Phadikar, Nonlocal elasticity theory for vibration of nanoplates, Journal of Sound and Vibration 325 (2009) 206–223. https://doi.org/10.1016/j.jsv.2009.03.007.

[11] A.C. Eringen, D.G.B. Edelen, On nonlocal elasticity, International Journal of Engineering Science 10 (1972) 233–248. https://doi.org/10.1016/0020-7225(72)90039-0.

[12] N. Challamel, C.M. Wang, The small length scale effect for a non-local cantilever beam: a paradox solved, Nanotechnology 19 (2008) 345703. https://doi.org/10.1088/0957-4484/19/34/345703.

[13] J. Peddieson, G.R. Buchanan, R.P. McNitt, Application of nonlocal continuum models to nanotechnology, International Journal of Engineering Science 41 (2003) 305–312. https://doi.org/10.1016/S0020-7225(02)00210-0.

[14] G. Romano, R. Barretta, Nonlocal elasticity in nanobeams: the stress-driven integral model, International Journal of Engineering Science 115 (2017) 14–27. https://doi.org/10.1016/j.ijengsci.2017.03.002.

[15] X. Li, T. Ono, Y. Wang, M. Esashi, Ultrathin single-crystalline-silicon cantilever resonators: Fabrication technology and significant specimen size effect on Young's modulus, Applied Physics Letters 83 (2003) 3081–3083. https://doi.org/10.1063/1.1618369.

[16] R. Barretta, F. Marotti de Sciarra, Variational nonlocal gradient elasticity for nano-beams, International Journal of Engineering Science 143 (2019) 73–91. https://doi.org/10.1016/j.ijengsci.2019.06.016.

[17] W. Yang, S. Wang, W. Kang, T. Yu, Y. Li, A unified high-order model for size-dependent vibration of nanobeam based on nonlocal strain/stress gradient elasticity with surface effect, International Journal of Engineering Science 182 (2023) 103785. https://doi.org/10.1016/j.ijengsci.2022.103785.

[18] A. Caporale, H. Darban, R. Luciano, Nonlocal strain and stress gradient elasticity of Timoshenko nano-beams with loading discontinuities, International Journal of Engineering Science 173 (2022) 103620. https://doi.org/10.1016/j.ijengsci.2021.103620.

[19] R. Penna, L. Feo, G. Lovisi, Hygro-thermal bending behavior of porous FG nano-beams via local/nonlocal strain and stress gradient theories of elasticity, Composite Structures 263 (2021) 113627. https://doi.org/10.1016/j.compstruct.2021.113627.

[20] H. Darban, R. Luciano, A. Caporale, M. Basista, Modeling of buckling of nanobeams embedded in elastic medium by local-nonlocal stress-driven gradient elasticity theory, Composite Structures 297 (2022) 115907. https://doi.org/10.1016/j.compstruct.2022.115907.

[21] S. Wang, W. Ding, Z. Li, B. Xu, C. Zhai, W. Kang, W. Yang, Y. Li, A size-dependent quasi-3D model for bending and buckling of porous functionally graded curved nanobeam, International Journal of Engineering Science 193 (2023) 103962. https://doi.org/10.1016/j.ijengsci.2023.103962.

[22] J. Loya, J. López-Puente, R. Zaera, J. Fernández-Sáez, Free transverse vibrations of cracked nanobeams using a nonlocal elasticity model, Journal of Applied Physics 105 (2009) 044309. https://doi.org/10.1063/1.3068370.

[23] M. Soltanpour, M. Ghadiri, A. Yazdi, M. Safi, Free transverse vibration analysis of size dependent Timoshenko FG cracked nanobeams resting on elastic medium, Microsyst Technol 23 (2017) 1813–1830. https://doi.org/10.1007/s00542-016-2983-3.

[24] O. Rahmani, S. a. H. Hosseini, M.H. Noroozi Moghaddam, I. Fakhari Golpayegani, Torsional Vibration of Cracked Nanobeam Based on Nonlocal Stress Theory with Various Boundary Conditions: An Analytical Study, Int. J. Appl. Mechanics 07 (2015) 1550036. https://doi.org/10.1142/S1758825115500362.

[25] Ş.D. Akbaş, Forced vibration analysis of cracked nanobeams, J Braz. Soc. Mech. Sci. Eng. 40 (2018) 392. https://doi.org/10.1007/s40430-018-1315-1.

[26] A.I. Aria, M.I. Friswell, T. Rabczuk, Thermal vibration analysis of cracked nanobeams embedded in an elastic matrix using finite element analysis, Composite Structures 212 (2019) 118–128. https://doi.org/10.1016/j.compstruct.2019.01.040.

[27] A. Bahrami, A wave-based computational method for free vibration, wave power transmission and reflection in multi-cracked nanobeams, Composites Part B: Engineering 120 (2017) 168–181. https://doi.org/10.1016/j.compositesb.2017.03.053.

[28] J.A. Loya, L. Rubio, J. Fernández-Sáez, Natural frequencies for bending vibrations of Timoshenko cracked beams, Journal of Sound and Vibration 290 (2006) 640–653. https://doi.org/10.1016/j.jsv.2005.04.005.

[29] J. Loya, J. López-Puente, R. Zaera, J. Fernández-Sáez, Free transverse vibrations of cracked nanobeams using a nonlocal elasticity model, Journal of Applied Physics 105 (2009) 044309. https://doi.org/10.1063/1.3068370.

[30] M. Krawczuk, M. Palacz, W. Ostachowicz, The dynamic analysis of a cracked Timoshenko beam by the spectral element method, Journal of Sound and Vibration 264 (2003) 1139–1153. https://doi.org/10.1016/S0022-460X(02)01387-1.

[31] T.G. Chondros, A.D. Dimarogonas, J. Yao, Vibration of a beam with a breathing crack, Journal of Sound and Vibration 239 (2001) 57–67. https://doi.org/10.1006/jsvi.2000.3156.

[32] Y. Narkis, Identification of Crack Location in Vibrating Simply Supported Beams, Journal of Sound and Vibration 172 (1994) 549–558. https://doi.org/10.1006/jsvi.1994.1195.

[33] S.P. Lele, S.K. Maiti, Modelling of transverse vibration of short beams for crack detection and measurement of crack extension, Journal of Sound and Vibration 257 (2002) 559–583. https://doi.org/10.1006/jsvi.2002.5059.

[34] J. Wang, P. Qiao, Vibration of beams with arbitrary discontinuities and boundary conditions, Journal of Sound and Vibration 308 (2007) 12–27. https://doi.org/10.1016/j.jsv.2007.06.071.

[35] S. Hadian Jazi, M. Hadian, K. Torabi, An exact closed-form explicit solution of free transverse vibration for non-uniform multi-cracked beam, Journal of Sound and Vibration 570 (2024) 117986. https://doi.org/10.1016/j.jsv.2023.117986.

[36] F. Cannizzaro, I. Fiore, A. Greco, S. Caddemi, I. Caliò, Eigenproperties of multi-cracked circular arches, Journal of Sound and Vibration 543 (2023) 117365. https://doi.org/10.1016/j.jsv.2022.117365.

[37] T. Yokoyama, M.-C. Chen, Vibration analysis of edge-cracked beams using a line-spring model, Engineering Fracture Mechanics 59 (1998) 403–409. https://doi.org/10.1016/S0013-7944(97)80283-4.

[38] P. Gudmundson, Eigenfrequency changes of structures due to cracks, notches or other geometrical changes, Journal of the Mechanics and Physics of Solids 30 (1982) 339–353. https://doi.org/10.1016/0022-5096(82)90004-7.

[39] H. Darban, Molecular Dynamics Benchmarks for Size-Dependent Tension, Bending, Buckling, and Vibration of Nanobeams, under review in International Journal of Engineering Science.

[40] F.P. Pinnola, S.A. Faghidian, R. Barretta, F. Marotti de Sciarra, Variationally consistent dynamics of nonlocal gradient elastic beams, International Journal of Engineering Science 149 (2020) 103220. https://doi.org/10.1016/j.ijengsci.2020.103220.

[41] H. Darban, R. Luciano, M. Basista, Free transverse vibrations of nanobeams with multiple cracks, International Journal of Engineering Science 177 (2022) 103703. https://doi.org/10.1016/j.ijengsci.2022.103703.